Elasticity of hydrous ringwoodite at mantle conditions: Implication for water distribution in the lowermost mantle transition zone

Wenzhong Wang[1,2], Han Zhang[3], John P. Brodholt[2,4], Zhongqing Wu[1,5,6]

[1]Laboratory of Seismology and Physics of Earth's Interior, School of Earth and Space Sciences, University of Science and Technology of China, Hefei, Anhui 230026, China

[2]Department of Earth Sciences, University College London, London WC1E 6BT, United Kingdom

[3]Department of Earth and Planetary Sciences, University of New Mexico, Albuquerque, NM, USA

[4]Centre for Earth Evolution and Dynamics, University of Oslo, Oslo, Norway

[5]National Geophysical Observatory at Mengcheng, University of Science and Technology of China, Hefei, China

[6]CAS Center for Excellence in Comparative Planetology, USTC, Hefei, Anhui 230026, China

Abstract

The mantle transition zone (MTZ) is potentially a geochemical water reservoir because of the high H_2O solubility in its dominant minerals, wadsleyite and ringwoodite. Whether the MTZ is wet or dry fundamentally impacts our understanding of the deep-water distribution, geochemical recycling, and the pattern of mantle convection. However, the water content in the MTZ inferred from previous studies remains disputed. Seismic observations such as velocity anomalies were used to evaluate the water content in the MTZ, but the hydration effect on the velocities of MTZ minerals under appropriate pressure (P) and temperature (T) conditions is poorly constrained. Here we investigated the elastic properties and velocities of hydrous ringwoodite at high P-T conditions using first-principles calculations. Our results show that the hydration effects on elastic moduli and velocities of ringwoodite are significantly reduced by pressure but strongly enhanced by temperature. The incorporation of 1.0 wt% water into ringwoodite decreases the compressional and shear velocities of the pyrolitic mantle by -1.0% and -1.4% at the conditions of MTZ, respectively. Using results from seismic tomography and together with the topography of the 660-km discontinuity, we evaluate the global distribution of water in the lower MTZ. We find that about 80% of the MTZ can be explained by varying water content and temperature, however, the remaining 20% requires the presence of high-velocity heterogeneities such as harzburgite. Our models suggest an average water concentration of ~0.2 wt% in the lower MTZ, with an interregional variation from 0 to 0.9 wt%. Together with our previous work, we conclude that the water concentration in the MTZ likely decreases with depth globally and the whole MTZ contains the equivalent of about one ocean mass of water.

Keywords: elasticity of hydrous ringwoodite, first-principles calculations, mantle transition zone, water content

1. Introduction

Earth's mantle transition zone (MTZ) is the region between 410 and 660 km and is mainly composed of wadsleyite, ringwoodite, and majorite. It separates the upper mantle from the lower mantle and plays an important role in mantle flow and slab subduction processes (Ballmer et al., 2015; Bercovici and Karato, 2003). It is widely accepted that the MTZ is potentially a large reservoir of water because wadsleyite and ringwoodite can store more than one weight percent of water in the form of hydroxyl (Fei and Katsura, 2020; Inoue et al., 2010, 1995; Jacobsen et al., 2005; Ohtani, 2015; Smyth, 1987). The discovery of a hydrous ringwoodite inclusion with ~1.4 wt% water in a natural 'superdeep' diamond from Brazil (Pearson et al., 2014) confirms experimental results and implies that the MTZ is at least locally hydrated. Such an interpretation is also supported by the findings of ice-VII inclusions in natural 'superdeep' diamonds (Tschauner et al., 2018), although again these inclusions are unlikely to be representative of the whole MTZ.

The actual amount of water and its spatial distribution in the MTZ are of great importance for understanding the structure and chemical composition of the deep mantle (Bercovici and Karato, 2003; Schmandt et al., 2014; Tauzin et al., 2010). Many studies have devoted significant effort to constraining the realistic hydration state of the MTZ based on electrical conductivity (Huang et al., 2005; Munch et al., 2020; Yoshino et al., 2008), but the estimated water concentration differs by more than one order of magnitude between these studies. For instance, some studies suggested a nearly anhydrous MTZ (Yoshino et al., 2008), whereas others argued that the MTZ is substantially more hydrated (Huang et al., 2005; Irifune, 1998; Karato, 2011; Kelbert et al., 2009), although even these studies do not agree on how much water the MTZ contains. This disagreement is probably due to large uncertainties in both the magnetotelluric observations and the experimentally measured electrical conductivity of MTZ minerals. In contrast to previous studies on conductivity, a nearly water-saturated MTZ model was recently proposed by comparing mineral viscosity data with the observed mantle viscosity profile (Fei et al., 2017). In addition, the seismic detection of partial melting above 410 km or below 660 km has also been used to infer regional-scale water variability (Schmandt et al., 2014; Tauzin et al., 2010; Wei and Shearer, 2017). Seismic observations of the variation in the depths of the 410-km and 660-km discontinuities have also been exploited in order to constrain the water content of the MTZ. This is because the pressure of the olivine to wadsleyite and the post-spinel phase transitions responsible for the 410 and 660 km discontinuities respectively vary with water content (Higo et al., 2001; Wood, 1995). Again, conflicting conclusions were obtained by different studies (Blum and Shen, 2004; Gao et al., 2010; Houser, 2016; Meier et al., 2009), probably because the transition pressures are also significantly affected by temperature.

Because the incorporation of water lowers the sound velocities of minerals, the observed seismic velocities in the MTZ can potentially be used to estimate its water content. For instance, in a pyrolitic mantle, wadsleyite should contain ~0.9 wt% water at the top of the MTZ to match both the density and seismic velocity jumps across the 410-km discontinuity (Wang et al., 2019). In principle, the density and velocity jumps across the 660-km discontinuity could also be used to infer the water content in the lower part of the MTZ. However, the complexity of phase transitions at ~ 660 km (Hirose, 2002) hampers the accurate estimate of the relationship between velocity contrasts and ringwoodite hydration. Instead, multiple seismic observations such as the depth of the 660-km discontinuity and the seismic velocity anomalies within the MTZ have been combined together to infer the hydration state of the MTZ, but yet again there is a large discrepancy in the amount of water between different studies (Houser, 2016; Mao et al., 2012; Schulze et al., 2018; Suetsugu et al., 2006).

One possible explanation for why so many studies using similar seismic observations of the transition zone come to different conclusions is that the effect of hydration on seismic wave velocities has not been well quantified. Experimental studies have reported the elastic properties and/or sound velocities of hydrous ringwoodite up to 22 GPa but only up to 673 K (Jacobsen and Smyth, 2006; Mao et al., 2012; Schulze et al., 2018; Wang et al., 2006). Moreover, even the results at ambient conditions can differ markedly between different studies (Mao et al., 2012; Schulze et al., 2018). Extrapolating results to different pressures and temperature is also problematic. For instance, Schulze et al. (2018) suggested that the hydration effect on the sound velocities of ringwoodite may be significantly weakened by pressure, while Mao et al. (2012) argued that temperature may strongly enhance the hydration-induced velocity reduction for compressional wave velocities of ringwoodite. This implies that extrapolation of low-temperature data to the P-T conditions of the MTZ could result in large uncertainties and contradictory conclusions.

In this study, we investigate the elastic properties and velocities of hydrous ringwoodite at the P-T conditions of the MTZ using first-principles calculations with the same computational details as those in our previous studies for the elasticity of anhydrous ringwoodite (Núñez Valdez et al., 2012) and wadsleyite (Núñez-Valdez et al., 2013; Wang et al., 2019). Together with elastic data for anhydrous ringwoodite (Núñez Valdez et al., 2012), we obtain the reduction in velocities of ringwoodite due to water over a wide range of pressures and temperatures and use that to quantify the effect of water on the velocities of a pyrolitic mantle at MTZ conditions. Combining mineral physics with seismological observations, we then estimate the water concentration and temperature anomaly in the lower MTZ using Monte Carlo simulations.

2. Method

Following Barron and Klein (1965), elastic constants can be derived from the relationship between the Helmholtz free energy and strain:

$$C_{ijkl}^{T} = \frac{1}{V}\left(\frac{\partial^2 F}{\partial e_{ij}\partial e_{kl}}\right) + \frac{1}{2}P(2\delta_{ij}\delta_{kl} - \delta_{il}\delta_{kj} - \delta_{ik}\delta_{jl}) \quad (1)$$

Here, $e_{ij}\ (i,j = 1,3)$ are infinitesimal strains, P is pressure, δ_{ij} refers to the Kronecker delta symbol, and F is the Helmholtz free energy. Within the quasi-harmonic approximation (QHA), F can be written as:

$$F(e_{ij},V,T) = U(e_{ij},V) + \frac{1}{2}\sum_{q,m}\hbar\omega_{q,m}(e_{ij},V)$$

$$+k_B T\sum_{q,m} ln\{1 - exp[-\frac{\hbar\omega_{q,m}(e_{ij},V)}{k_B T}]\} \quad (2)$$

where V is equilibrium volume and T is temperature. Parameters ω, q, and m represent the vibrational frequencies, the phonon wave vector, and the normal index, respectively. $\hbar$, k_B are reduced Planck and Boltzmann constants. The first, second, third terms in Eq. (2) are the static internal, zero-point, and vibrational energy contributions, respectively. As such, this conventional method requires the calculations of vibrational properties of many strained configurations, which requires significant computational effort. Wu and Wentzcovitch (2011) developed a semi-analytical method that only needs the vibrational properties of unstrained configurations to calculate the high P-T elasticity, which consequently reduces the computational work to the level of less than one-tenth of the conventional method. This approach has been successfully applied to the thermal elasticity of many minerals (Duan et al., 2019; Hao et al., 2019; Hu et al., 2016; Núñez-Valdez et al., 2013; Núñez Valdez et al., 2012; Qian et al., 2018; Shukla et al., 2016, 2015; Wang et al., 2019, 2020; Wang and Wu, 2018; Wu et al., 2013; Wu and Wang, 2016; Wu and Wentzcovitch, 2011; Yang et al., 2017; Yang and Wu, 2014; Zou et al., 2018), and so we use it to obtain the elastic properties of hydrous ringwoodite at high P-T conditions in this study. The adiabatic bulk modulus K_S and shear modulus G are obtained by using the Voigt-Reuss-Hill averages, and compressional wave velocity (V_P) and shear wave velocity (V_S) are from elastic moduli and density using $V_P = \sqrt{(K_S + \frac{4}{3}G)/\rho}$ and $V_S = \sqrt{G/\rho}$.

First-principles calculations were performed using the Quantum Espresso package (Giannozzi et al., 2009) based on the density functional theory (DFT), adopting the local density approximation (LDA) for the exchange-correlation function, unless noted otherwise. The pseudopotentials of Mg, Si, H, and O are described in our previous studies (Duan et al., 2019; Hu et al., 2016; Wang et al., 2019). The cutoff energy for the plane wave was 70 Ry. The structures of hydrous ringwoodite were optimized under different pressures using the variable cell-shape damped molecular dynamics approach (Wentzcovitch, 1991) with a 2×2×2 k-point mesh. The dynamical matrices for relaxed structures were calculated using density functional-perturbation theory (DFPT) (Baroni et al., 2001) with a 2×2×2 q-point mesh and were extrapolated to a denser q mesh to obtain the vibrational density of states. Elastic tensors at static conditions were calculated from the stress-strain relationship. The calculated Helmholtz free energy versus volume was fitted by the isothermal third-order finite strain equation of state, which was used to calculate thermodynamic parameters including pressure. The volume versus pressure relationship was fitted by the Birch-Murnaghan third-order equation of state.

Dry ringwoodite ($^{IV}A^{VI}B_2O_4$) has a normal spinel structure with space group Fd-3m, in which the six-coordinated B site (16d) is occupied by Mg atom and the four-coordinated A site (8a) is occupied by Si atom. There are three possible mechanisms for the incorporation of hydrogen into ringwoodite (Blanchard et al., 2009; Li et al., 2009; Panero, 2010): (1) V_{Mg}'' +2H**, which is a Mg vacancy charge balanced by two H atoms; (2) V_{Si}'''' +4H****, a Si vacancy charge balanced by four H atoms; (3) Mg_{Si}'' +2H**, a Si vacancy occupied by a Mg atom charge balanced by two H atoms. Previous first-principles calculations (Panero, 2010) found that these three substitution mechanisms exist in ratios of 65:25:10 respectively, and so hydrogen is mainly incorporated into ringwoodite through the mechanism V_{Mg}'' +2H** (Hernández et al., 2013). Results of fitting experimental data on hydrous ringwoodite also show that the three defects exist in a ratio of 75:14:11 (Panero, 2010). This is also supported by more recent experimental results from nuclear resonance spectroscopy (Grüninger et al., 2017). Thus, we adopt the substitution mechanism V_{Mg}'' +2H** to construct the initial structure of hydrous ringwoodite with 1.63 wt% water ($Mg_{15}Si_8O_{30}(OH)_2$), where the sites for two H atoms were determined by following the experimental results from pulsed neutron diffraction (Purevjav et al., 2014) (Fig. S1). In order to estimate the effect of the mechanisms (2) and (3), we calculated the elastic properties of hydrous ringwoodite with the substitution V_{Si}'''' +4H**** and Mg_{Si}'' +2H** at static conditions (Table S1). Our results show that the relative difference in the elastic moduli and sound velocities of hydrous ringwoodite between the mechanism (1) and the mixing mechanism with the ratios of 65:25:10 and/or 75:14:11 is less than 0.4% at the pressures of MTZ.

At ambient pressure, the calculated frequencies of OH stretching modes are ~2250 cm^{-1}, lower than the experimental measurements (Thomas et al., 2015 and references therein), although the experimental infrared spectrum of hydrous ringwoodite consists of several broad bands for OH stretching modes. This is mainly because the LDA overestimates the H-O bond lengths and there are different hydration mechanisms involved in experimental samples (Li et al., 2009). However, vibrational frequencies of dry ringwoodite can be well predicted by the LDA (Wu et al., 2015). Although the generalized gradient approximation (GGA) is better than LDA for predicting the H-O bonding, LDA is more suitable for calculating elastic properties of many silicate minerals including hydrous wadsleyite (Wang et al., 2019). In order to check the influence of the exchange-correlation function on the hydration effect in ringwoodite, we also calculated the elastic properties of ringwoodite using the GGA at static conditions (Table S2). The results show that the water effects on elastic moduli and velocities of ringwoodite predicted by the GGA are similar to those from the LDA calculations (Table S2).

Experiments show that the incorporation of hydrogen into ringwoodite does not affect its space group symmetry, suggesting a disordered distribution of Mg vacancies. In contrast, the presence of a Mg vacancy in $Mg_{15}H_2Si_8O_{32}$ ringwoodite breaks its high symmetry in our calculations. In order to account for the effect of disorder, we averaged the elastic constants over all possible symmetrically equivalent sites for Mg vacancy by following the method used in Núñez-Valdez et al. (2010), and the final elastic tensor has the Fd-3m symmetry and can be fully described by C_{11}, C_{12}, and C_{44}.

3. Results

3.1 Elasticity of hydrous ringwoodite at high P-T conditions

The elastic properties, density, and sound velocities of hydrous ringwoodite with 1.63 wt% H_2O ($Mg_{15}H_2Si_8O_{32}$) at high P-T conditions are shown in Fig. 1 and their fitting parameters are reported in Table S3 and Table S4. At ambient conditions, C_{11}, C_{12}, C_{44}, K_S, and G of $Mg_{15}H_2Si_8O_{32}$ ringwoodite are 8-10% lower than those of Mg_2SiO_4 ringwoodite (Núñez Valdez et al., 2012). Elastic moduli show noticeable nonlinear dependences on pressure, which consequently results in nonlinear pressure dependences of sound velocities (Fig. 1). At 300 K, the first pressure derivatives of K_S, G, V_P, and V_S ($\partial K_S/\partial P$, $\partial G/\partial P$, $\partial V_P/\partial P$, and $\partial V_S/\partial P$) decrease from 4.72, 1.53, 0.0735 km s^{-1} GPa^{-1}, and 0.0231 at km s^{-1} GPa^{-1} 0 GPa to 4.11, 0.73, 0.0404 km s^{-1} GPa^{-1}, and 0.0043 km s^{-1} GPa^{-1} at 20 GPa, respectively. In contrast, the elastic moduli and wave velocities show almost linear dependences on temperature, but the temperature effect at high pressure is much weaker than that at low pressure (Fig. 1). The first temperature derivatives of K_S, G, V_P, and V_S ($\partial K_S/\partial T$, $\partial G/\partial T$, $\partial V_P/\partial T$, and $\partial V_S/\partial T$) change from -24.1 MPa/K, -14.5 MPa/K, -0.523×10^{-3} km s^{-1} K^{-1}, and -0.297×10^{-3} km s^{-1} K^{-1} at 0 GPa to -18.1 MPa/K, -8.7 MPa/K, -0.275×10^{-3} km s^{-1} K^{-1}, and -0.143×10^{-3} km s^{-1} K^{-1} at 20 GPa. The elastic moduli and sound velocities of hydrous wadsleyite with 1.63 wt% water also show nonlinear dependences on pressure but almost linear dependences on temperature, and the temperature effect also noticeably reduces at high pressure compared to that at low pressure (Wang et al., 2019). The pressure and temperature derivatives of elastic moduli and wave velocities of $Mg_{15}H_2Si_8O_{32}$ ringwoodite are also comparable with those of $Mg_{15}H_2Si_8O_{32}$ wadsleyite (Wang et al., 2019). As such, extrapolating low P-T experimental data to high P-T conditions needs to consider these nonlinear pressure effects.

3.2 Comparisons between theoretical and experimental results

In order to compare our results for hydrous ringwoodite with the experimental measurements, the elastic moduli and density are interpolated linearly from ringwoodite with 1.63 wt% water to the previously calculated elasticity of anhydrous ringwoodite (Núñez Valdez et al., 2012) (Fig. S2). Similarly, the effect of iron on the elastic moduli and density are also taken into account using the linear interpolation from the results of Fe-bearing to Fe-free ringwoodite (Núñez Valdez et al., 2012). The combined effects of iron and water content on elastic moduli and density of ringwoodite are estimated by adding the two separate effects together. This strategy is also supported by previous experimental measurements for hydrous Fo89 (Fo, the Mg_2SiO_4 fraction) and Fo100 ringwoodite (Schulze et al., 2018; Wang et al., 2006), which show that the hydration effect is independent of the presence of iron in ringwoodite. Meanwhile, by fitting large datasets of experimental results, Wang et al. (2018) also found co-linear dependences between elastic moduli of ringwoodite and Fe and H_2O concentrations. Similarly, previous theoretical and experimental studies also found that the incorporation of H_2O shows similar reductions on the elastic moduli of Fe-free and Fe-bearing wadsleyite (Wang et al., 2019).

The calculated density and elastic properties of hydrous ringwoodite with variable iron and water contents are compared with experimental results in Fig. 2 and Fig. 3, respectively. Our results for the density of hydrous ringwoodite show excellent agreement with previous experimental data (Chang et al., 2015; Jacobsen et al., 2004; Jacobsen and Smyth, 2006; Mao et al., 2012; Schulze et al., 2018; Wang et al., 2006; Ye et al., 2012), with a discrepancy between theoretical and experimental results of less than 1.3% (Fig. 2). This small difference is likely caused by two factors: the mild underestimated volume from LDA calculations (Núñez-Valdez et al., 2013; Núñez Valdez et al., 2012; Wang et al., 2019) and the uncertainties of iron and water contents in experimental samples (Chang et al., 2015). Nevertheless, these comparisons present strong evidence for the reliability of our calculations.

The predicted elastic moduli of hydrous ringwoodite also show good agreements with the experimental results of Jacobsen and Smyth (2006) and Wang et al. (2006) at different pressures and 300 K (Fig. 2a and 2b). Experimental results from two Brillouin spectroscopy studies (Mao et al., 2012; Schulze et al., 2018) are in marked disagreement on elastic moduli and sound velocities, especially at high pressures. Although the measured G of hydrous ringwoodite in Mao et al. (2012) is consistent with our results, K_S deviates from our theoretical predictions at high pressure (Fig. 2c). In contrast, the comparison between this work and Schulze et al. (2018) suggests a good agreement in K_S, but the measured G of ringwoodite, especially for Fo89 ringwoodite with 1.04 wt% and 1.71 wt% water, is slightly larger than our predictions (Fig. 2d). It should be noted that experimental values in Schulze et al. (2018) have significant scatter (Fig. 2d), but as well as the experimental uncertainty, the discrepancies in G may also be due to the slightly different dependences of G on iron content between experimental and theoretical studies (Núñez Valdez et al., 2012). In contrast, experimental and theoretical studies are in better agreement over the effect of iron on ringwoodite K_S, while the results of Mao et al. (2012) show marked disagreement with the results of this study and Schulze et al. (2018). It has also been suggested that different mechanisms for hydrogen incorporation between the studied ringwoodite samples – possibly caused by differences in the synthesis procedure – may be responsible for the discrepancies between experiments (Schulze et al., 2018). However, as discussed earlier, hydrogen is mostly incorporated into ringwoodite through the substitution mechanism V_{Mg}''+2H** (Grüninger et al., 2017; Panero, 2010), which is also supported by the chemical compositions of ringwoodite samples (Jacobsen and Smyth, 2006; Mao et al., 2012; Schulze et al., 2018; Wang et al., 2006) and the dependence of volume on hydration (Schulze et al., 2018). The main reasons for the discrepancies between this study and some experiments and between different experiments are unclear, and further well-designed experiments are needed to clarify this problem.

3.3 Water effect on the elastic moduli and velocities of ringwoodite

The current calculations were conducted using the same computational methods, as far as possible, as in previous works on the elasticity of anhydrous hydrous (Núñez Valdez et al., 2012). Together, these calculations provide self-consistent and high-quality data to quantify the hydration effect on elasticity and wave velocities of ringwoodite at high P-T conditions without extrapolation. Our results show that at ambient conditions one weight percent of water dissolved into ringwoodite reduces K_S and G by 5.1% and 6.0%, respectively, consistent with previous experimental observations within uncertainty (Jacobsen and Smyth, 2006; Mao et al., 2012; Schulze et al., 2018; Wang et al., 2006). These reductions in K_S and G result in a 2.3% decrease in V_P and a 2.5% decrease in V_S, which also agree well the recent experimental data (Table S5, Schulze et al., 2018). Such a hydration effect on elastic moduli and wave velocities of ringwoodite is similar to that of wadsleyite (Wang et al., 2019).

Compared to ambient pressure, the effect of water on lowering elastic moduli and sound velocities of ringwoodite is reduced at high pressures (Fig. 4 and Fig. S2-S3). At 25 GPa and 300 K, the presence of 1.0 wt% water in ringwoodite only decreases K_S, G, V_P, and V_S by 1.4%, 3.2%, 0.7%, and 1.3%, respectively. The recent experimental and theoretical works (Buchen et al., 2018; Schulze et al., 2018; Wang et al., 2019) also found a significant decrease in the hydration effect on elastic properties and sound velocities in ringwoodite and wadsleyite. However, the hydration effect is strongly enhanced at elevated temperatures (Fig. 4 and Fig. S2-S3). At 25 GPa and 2000 K, the reductions in K_S, G, V_P, and V_S are increased to 3.3%, 4.8%, 1.7%, and 2.2%, respectively, which are much greater than those at 25 GPa and 300 K. Similar results have also been found in wadsleyite (Wang et al., 2019). Thus, we conclude that the hydration effect on elastic moduli and wave velocities of nominally anhydrous minerals at low P-T conditions cannot be simply applied to the mantle conditions, and the extrapolation may cause large uncertainties.

4. Discussion

4.1 Hydration effect on velocity reductions in a pyrolitic mantle

Combining our results with previous studies (Gréaux et al., 2019; Irifune et al., 2008; Núñez Valdez et al., 2012), we estimated the hydration effect on the wave velocities of a pyrolitic mantle (58% ringwoodite (10 mol% Fe) + 35% majorite (the ‘pyrolite minus olivine’ composition) + 7% calcium perovskite) (Irifune et al., 2010) as a function of water content in ringwoodite and temperature anomaly at the conditions of the lower MTZ (Fig. 5). Here we do not consider the hydration effect in majorite because its water solubility does not exceed 0.1 wt% (Ohtani, 2015), which should be a negligible effect on the modeling results. We find that the incorporation of 1.0 wt% water into ringwoodite would decrease the sound velocities of the pyrolitic mantle by -1.0% in V_P and -1.4% in V_S at the conditions of the lower MTZ (Fig. 5). Such ΔV_P and ΔV_s magnitudes can be also produced by increasing the temperature by 230 K (Fig. 5), showing that the presence of a negative temperature anomaly can make the hydration effect invisible. In addition, the presence of 0.2 wt% water in ringwoodite can only produce ΔV_P and ΔV_s anomalies of -0.3%, so it is unlikely that such small amounts of water can be identified by seismic observations (Houser, 2016).

Schulze et al. (2018) also estimated the dependence of velocity reduction in a pyrolitic mantle on ringwoodite hydration and found that the V_S would only decrease by about 0.3% for the incorporation of 1.0 wt% water into ringwoodite at the conditions of the MTZ. This value is much lower than our results, mainly because they assumed the effect of water on the elastic moduli of ringwoodite at ambient temperature would be appropriate at the temperature of the MTZ. Instead, the hydration effect is strongly enhanced by increasing temperature (Fig. 4 and Fig. S2-S3). Mao et al. (2012) predicted that the presence of 1.0 wt% water in ringwoodite would decrease V_P and V_S by 7.0% and 4.5% at the conditions of the lower MTZ, respectively. Such velocity reductions lead to a ΔV_P of about -4.2% and a ΔV_S of -2.5% for a pyrolitic composition, much larger than our predictions. This again is due to the significant differences in the results of hydrous ringwoodite between this study and Mao et al. (2012) (Fig. 3) and a large extrapolation to MTZ conditions.

We also estimated the effects of ringwoodite hydration and temperature on the V_P/V_S ratio for a pyrolitic composition (Fig. S4). Our results show that the incorporation of 1.0 wt% water into ringwoodite only increases the V_P/V_S ratio of pyrolite by ~0.3%, suggesting that the V_P/V_S anomaly ($\Delta(V_P/V_S)$) is not significantly sensitive to water content. Previous seismological work (Li et al., 2013) found a V_P/V_S anomaly of > +2.1% in the lower MTZ beneath Northeast China and ascribed it as a result of hydrous MTZ. However, according to our results, such a $\Delta(V_P/V_S)$ cannot be caused by the presence of water in the MTZ, and other reasons such as the partial melting induced by upwelling (Tang et al., 2014) may account for the high V_P/V_S ratio. The hydration state of the MTZ would certainly be hard to identify by the $\Delta(V_P/V_S)$.

4.3 Mapping the amount of water in the lower MTZ

The presence of water lowers the seismic velocities (Fig. 5) and deepens the 660-km discontinuity simultaneously (Higo et al., 2001). Increasing temperature also results in negative velocity anomalies, but in contrast to water, temperature will elevate the 660-km discontinuity to shallower depths (Bina and Helffrich, 1994; Fei et al., 2004; Higo et al., 2001; Irifune, 1998; Yu et al., 2007). Thus, the observed topography of the 660-km discontinuity and seismic velocity anomalies in the lower MTZ could result from the combined effects of water amount and temperature variations.

In order to constrain the water content in the MTZ, Houser (2016) compared the topography of the 410- and 660-km discontinuities and shear wave velocities within the MTZ, with literature mineral physics data. That work concluded that the transition is mostly dry. However, several problems exist with the mineral physics used in that study. First, as we point out above, the extrapolation of experimental data at low temperature to the MTZ's temperature may lead to large uncertainties in estimating the hydration effect on ringwoodite's sound velocities. And, as discussed in section 4.1 and 4.2, significant differences in hydration effect exist between different experimental studies. Second, Houser (2016) used the hydration effect on ringwoodite rather than that on pyrolite to estimate the relationship between ΔV_S and water content; this alone is likely to bias the results to systematically lower water contents. Third, the temperature profile of the transition was assumed to be the same everywhere. These shortcomings may account for the inference that very few seismic observations match the predictions from mineral physics in Houser (2016). Even for these locations where seismic observations could be explained by the presence of water, the water concentration from the topography of the 660-km discontinuity is different from the one from the shear wave velocity anomalies (Houser, 2016).

We therefore decided to use our elastic data calculated in this work with the seismic observations in Houser (2016) to map out the water concentration in the lower MTZ. The seismic observations on the depth variation of the 660-km discontinuity (Δd) and the V_S anomalies (ΔV_S) in the lower MTZ are taken as targets to match. Unlike Houser (2016), we do not also use the depth variation of the 410-km discontinuity (which also depends on water content and temperature) as one of the constraints because the hydration state of the MTZ may vary with depth. The dependence of ΔV_S on water content and temperature expected in pyrolite are derived from our study, and the effects of water and temperature on the depth of the 660-km discontinuity are determined using literature data. The temperature effect on the depth of the 660-km discontinuity is adopted as −0.06 km/K and the effect of ringwoodite hydration on the depth of the 660-km discontinuity is adopted as +6 km/wt% (Higo et al., 2001, Fig. S5). Solutions for water content and temperature anomaly were determined using a Monte Carlo simulation, in which 70000 initial inputs were randomly produced in the ranges of 0-1.6 wt% for water content and -800-+800 K for temperature anomaly. The outputs were kept if they match the observed ΔV_S within 0.3% and Δd within 3 km (Fig. S6). The final amount of water in the lower MTZ is estimated by the product of water content in ringwoodite and the fraction of ringwoodite (58%).

We found that ~79% of the bins that have observations of both ΔV_S and Δd (blue areas in Fig. 6a) can be satisfied by a pyrolitic mantle with variable amounts of water and temperature. We also find that the water concentration within 57% of the bins exceeds 0.1 wt% (Fig. 8). In contrast, Houser (2016) found that only 8% of the bins with high-quality data are consistent with the presence of water based on the same seismic observations, but the water concentration estimated from ΔV_S is much lower than the one constrained from Δd. Our modeling results show that the water concentration and temperature anomaly in the lower MTZ vary from 0 to 0.9 wt% and from -350 K to +350 K (Fig. 7), respectively. The average temperature anomaly is -29±21 K and the average water concentration is 0.25±0.06 wt%. If the remaining 21% of bins are dry, the lower MTZ is somewhat hydrous, with about 0.2±0.04 wt% water. As discussed above, the difference between our results and those of Houser (2016) is probably due to the mineral physics data and because we allowed the temperature of the transition zone to vary laterally.

Globally, there is no evident correlation between the modeled water concentration and temperature anomaly, but the maximum water concentration decreases with increasing temperature anomaly (Fig. S7) and does not exceed the water solubility in ringwoodite determined by experimental studies (Fei and Katsura, 2020 and references therein). The temperature anomaly and the water content in the lower MTZ vary by region. In general, the temperature anomaly in the western Pacific ranges from -300 K to -50 K, while the central and eastern Pacific is somewhat hotter. The lower MTZ beneath the Philippine Sea and the Hawaiian Islands, and North Asia is quite hydrous, which is also supported by the high conductivity anomalies beneath these regions (Shimizu et al., 2010). In particular, the high conductivity beneath the Philippine Sea cannot be explained only by the temperature effect and the region would contain 0.5-1.0 wt% water in the lower MTZ (Shimizu et al., 2010), if the cause of the high conductivity is due to the presence of water. Such an estimate is consistent with our model (Fig. 7a). In addition, other studies (Kelbert et al., 2009; Munch et al., 2018; Semenov and Kuvshinov, 2012) also found high conductivity anomalies in the lower MTZ beneath North Asia, which can be explained by our predicted water amount in this region (Fig. 7a). The substantial amount of water in the lower MTZ beneath these local regions may have resulted in seismic anomalies at the top of the lower mantle if there is a downward flow (Bercovici and Karato, 2003; Schmandt et al., 2014), which might be detected by further seismic studies.

The remaining 21% of bins where ΔV_S and Δd cannot be explained by our models (red areas in Fig. 6a) can be divided into three groups: (1) $-\Delta d$, $+\Delta V_S$; (2) $-\Delta d$, $-\Delta V_S$; (3) $+\Delta d$, $+\Delta V_S$. In principle, the pattern of ($-\Delta d$, $+\Delta V_S$) cannot be produced by the variations in water content and temperature because $-\Delta d$ can be only produced by the positive temperature anomaly, which cannot produce $+\Delta V_S$ with or without water. For the regions with ($-\Delta d$, $-\Delta V_S$) and ($+\Delta d$, $+\Delta V_S$), the Δd within these bins could be caused by temperature anomalies, but the observed ΔV_S exceeds the range predicted by mineral physics and the presence of water will widen the ΔV_S difference between seismic observations and mineral models even further (Fig. 6b). Thus, these bins cannot be matched by varying water content and temperature within reasonable ranges and require high-velocity heterogeneities to explain their ΔV_S. Harzburgite, which is composed of ~80% ringwoodite and 20% majorite at the conditions of the MTZ, is found to have higher velocities than pyrolite in the lower MTZ (Gréaux et al., 2019) and could be a candidate for such heterogeneities. However, we cannot rule out the possibility of the presence of heterogeneities in other regions where the seismic observations are consistent with the current mineral models. If there is harzburgite, more water is needed to explain the observed ΔV_S (Fig. 6b).

We also find similar results for the hydration state of the lower MTZ using other seismic models. For instance, using the topography of the 660-km discontinuity from Guo and Zhou (2020) and shear wave velocity anomaly within the lower MTZ from the S40RTS model (Ritsema et al., 2011), most of the bins with observations of both ΔV_S and Δd can be explained by our models (Fig. S8) (84% in this case versus 79% above). The water concentration varies from 0 to 0.9 wt%, which is the same as with the Houser (2016) tomography, and the temperature anomaly is also similar, varying from -550 K to +300 K (Fig. S8). Despite some small-scale local mismatches due to the difference between the two seismic models, the average water concentration is 0.18±0.05 wt% and the average temperature anomaly is -23±26 K, both of which similar to the results inferred from Houser's seismic models.

Our results suggest that globally the lower MTZ is somewhat hydrous, with about 0.2±0.04 wt% water. Such an amount of water is consistent with the magnetotelluric model in Kelbert et al. (2009) within the uncertainty, although large discrepancies still exist between different magnetotelluric studies (Huang et al., 2005; Kelbert et al., 2009; Yoshino et al., 2008). Based on the mantle viscosity profile inferred from the postglacial rebound data, Fei et al. (2017) suggested a nearly water-saturated MTZ (1-2 wt% water), especially at the lowest reaches of the MTZ, significantly higher than the amount estimated in this study. This may be because the viscosity model predicted by mineral physics in Fei et al. (2017) did not consider the effect of majorite, which is one of the major minerals in the MTZ. Also, it should be noted that the viscosity profile for the MTZ inferred from the geoid and postglacial rebound data differs by one order of magnitude between independent studies (Čížková et al., 2012). As such, the viscosity may not be a good sensor for the water content in the MTZ.

Our previous work found that wadsleyite in a pyrolitic mantle should contain ~0.9 wt% water to match the density and seismic velocity jumps across the 410-km discontinuity, suggesting a hydrous uppermost MTZ with a water concentration of ~0.5 wt% (Wang et al., 2019). This implies that the water concentration in the MTZ may decrease with depth globally, from ~0.5 wt% in the upper part to ~0.15-0.2 wt% in the lower part, which may partly contribute to the observed velocity gradients in the MTZ (Thio et al., 2016). Accordingly, the MTZ contains about one ocean mass equivalent water.

5. Conclusion

We investigated the elastic properties and velocities of hydrous ringwoodite containing 1.63 wt% water at high P-T conditions using first-principles calculations within the LDA. Our results show that the elastic moduli of the hydrous ringwoodite are 8-10% lower than those of dry ringwoodite at ambient conditions. Elastic moduli and wave velocities show noticeable nonlinear dependences on pressure, with their pressure derivatives decreasing with increasing pressure. In contrast, the elastic moduli and wave velocities show almost linear dependences on temperature, but the temperature effect at high pressure is much weaker than that at low pressure. The calculated elastic moduli and density of hydrous ringwoodite with variable water contents agree well with most of the experimental data.

Our calculations were conducted using the same computational methods as in previous works on the elasticity of anhydrous ringwoodite (Núñez Valdez et al., 2012) and hence provided self-consistent and high-precision data to estimate the hydration effect on the elasticity and velocities of ringwoodite. At ambient conditions, one weight percent of water dissolved into ringwoodite reduces the K_S, G, V_P, and V_S by 5.1%, 6.0%, 2.3%, and 2.5%, respectively. The hydration effect is significantly reduced at high pressures but strongly enhanced at elevated temperatures. At 25 GPa and 2000 K, the reductions in K_S, G, V_P, and V_S caused by the presence of 1.0 wt% water are 3.3%, 4.8%, 1.7%, and 2.2%, respectively. Combining our results with previous studies, we find that the incorporation of 1.0 wt% water into ringwoodite would decrease the wave velocities of the pyrolitic mantle by -1.0% in V_P and -1.4% in V_S at MTZ conditions.

We evaluated the amount of water in the lower MTZ using the seismic observations on the depth variation of the 660-km discontinuity (Δd) and the V_S anomalies (ΔV_S) in the lower MTZ from previous seismic models. Most bins with ΔV_S and Δd can be matched by our models and the remaining bins require high-velocity heterogeneities such as harzburgite to explain their ΔV_S. The average water concentration in the lower MTZ is 0.2±0.04 wt%, with an interregional variation from 0 to 0.9 wt%. Together with our previous work on the water content in the upper MTZ (Wang et al., 2019), we suggest that the water concentration in the MTZ likely changes with depth globally and the whole MTZ contains about one ocean mass equivalent water.

Acknowledgments

This study is supported by the Natural Science Foundation of China (41590621, 41925017, 41721002) and the Special Program for Applied Research on Super Computation of the NSFC-Guangdong Joint Fund. This work was also supported by NERC grant NE/M00046X/1. The calculations were conducted partly at the supercomputing center of University of Science and Technology of China. We thank Dr. Zhou Ying (Department of Geosciences, Virginia Tech) for sharing the depth data of the 660-km discontinuity. We are grateful to the constructive comments from two anonymous reviewers and editorial handling by James Badro.

References

Ballmer, M.D., Schmerr, N.C., Nakagawa, T., Ritsema, J., 2015. Compositional mantle layering revealed by slab stagnation at 1000-km depth. Sci. Adv. 1, e1500815–e1500815. doi:10.1126/sciadv.1500815

Baroni, S., de Gironcoli, S., Dal Corso, A., Giannozzi, P., 2001. Phonons and related crystal properties from density-functional perturbation theory. Rev. Mod. Phys. 73, 515–562. doi:10.1103/RevModPhys.73.515

Barron, T.H.K., Klein, M.L., 1965. Second-order elastic constants of a solid under stress. Proc. Phys. Soc. 85, 523–532. doi:10.1088/0370-1328/85/3/313

Bercovici, D., Karato, S.-I., 2003. Whole-mantle convection and the transition-zone water filter. Nature 425, 39–44. doi:10.1038/nature01918

Bina, C.R., Helffrich, G., 1994. Phase transition Clapeyron slopes and transition zone seismic discontinuity topography. J. Geophys. Res. 99, 15853. doi:10.1029/94JB00462

Blanchard, M., Balan, E., Wright, K., 2009. Incorporation of water in iron-free ringwoodite: A first-principles study. Am. Mineral. 94, 83–89. doi:10.2138/am.2009.3020

Blum, J., Shen, Y., 2004. Thermal, hydrous, and mechanical states of the mantle transition zone beneath southern Africa. Earth Planet. Sci. Lett. 217, 367–378. doi:10.1016/S0012-821X(03)00628-9

Brown, J.M., Shankland, T.J., 1981. Thermodynamic parameters in the Earth as determined from seismic profiles. Geophys. J. Int. 66, 579–596. doi:10.1111/j.1365-246X.1981.tb04891.x

Buchen, J., Marquardt, H., Speziale, S., Kawazoe, T., Boffa Ballaran, T., Kurnosov, A., 2018. High-pressure single-crystal elasticity of wadsleyite and the seismic signature of water in the shallow transition zone. Earth Planet. Sci. Lett. 498, 77–87. doi:10.1016/j.epsl.2018.06.027

Chang, Y., Jacobsen, S.D., Bina, C.R., Thomas, S., Smyth, J.R., Frost, D.J., Boffa Ballaran, T., McCammon, C.A., Hauri, E.H., Inoue, T., Yurimoto, H., Meng, Y., Dera, P., 2015. Comparative compressibility of hydrous wadsleyite and ringwoodite: Effect of H 2 O and implications for detecting water in the transition zone. J. Geophys. Res. Solid Earth 120, 8259–8280. doi:10.1002/2015JB012123

Čížková, H., van den Berg, A.P., Spakman, W., Matyska, C., 2012. The viscosity of Earth's lower mantle inferred from sinking speed of subducted lithosphere. Phys. Earth Planet. Inter. 200–201, 56–62. doi:10.1016/j.pepi.2012.02.010

Duan, L., Wang, W., Wu, Z., Qian, W., 2019. Thermodynamic and Elastic Properties of Grossular at High Pressures and High Temperatures: A First-Principles Study. J. Geophys. Res. Solid Earth 124, 2019JB017439. doi:10.1029/2019JB017439

Fei, H., Katsura, T., 2020. High water solubility of ringwoodite at mantle transition zone temperature. Earth Planet. Sci. Lett. 531, 115987. doi:10.1016/j.epsl.2019.115987

Fei, H., Yamazaki, D., Sakurai, M., Miyajima, N., Ohfuji, H., Katsura, T., Yamamoto, T., 2017. A nearly water-saturated mantle transition zone inferred from mineral viscosity. Sci. Adv. 3, e1603024. doi:10.1126/sciadv.1603024

Fei, Y., Van Orman, J., Li, J., van Westrenen, W., Sanloup, C., Minarik, W., Hirose, K., Komabayashi, T., Walter, M., Funakoshi, K., 2004. Experimentally determined postspinel transformation boundary in Mg 2 SiO 4 using MgO as an internal pressure standard and its geophysical implications. J. Geophys. Res. Solid Earth 109, 1–8. doi:10.1029/2003JB002562

Gao, Y., Suetsugu, D., Fukao, Y., Obayashi, M., Shi, Y., Liu, R., 2010. Seismic discontinuities in the mantle transition zone and at the top of the lower mantle beneath eastern China and Korea: Influence of the stagnant Pacific slab. Phys. Earth Planet. Inter. 183, 288–295. doi:10.1016/j.pepi.2010.03.009

Giannozzi, P., Baroni, S., Bonini, N., Calandra, M., Car, R., Cavazzoni, C., Ceresoli, D., Chiarotti, G.L., Cococcioni, M., Dabo, I., Dal Corso, A., de Gironcoli, S., Fabris, S., Fratesi, G., Gebauer, R., Gerstmann, U., Gougoussis, C., Kokalj, A., Lazzeri, M., Martin-Samos, L., Marzari, N., Mauri, F., Mazzarello, R., Paolini, S., Pasquarello, A., Paulatto, L., Sbraccia, C., Scandolo, S., Sclauzero, G., Seitsonen, A.P., Smogunov, A., Umari, P., Wentzcovitch, R.M., 2009. QUANTUM ESPRESSO: a modular and open-source software project for quantum simulations of materials. J. Phys. Condens. Matter 21, 395502. doi:10.1088/0953-8984/21/39/395502

Gréaux, S., Irifune, T., Higo, Y., Tange, Y., Arimoto, T., Liu, Z., Yamada, A., 2019. Sound velocity of CaSiO3 perovskite suggests the presence of basaltic crust in the Earth's lower mantle. Nature 565, 218–221. doi:10.1038/s41586-018-0816-5

Grüninger, H., Armstrong, K., Greim, D., Boffa-Ballaran, T., Frost, D.J., Senker, J., 2017. Hidden Oceans? Unraveling the Structure of Hydrous Defects in the Earth's Deep Interior. J. Am. Chem. Soc. 139, 10499–10505. doi:10.1021/jacs.7b05432

Guo, Z., Zhou, Y., 2020. Finite-frequency imaging of the global 410- and 660-km discontinuities using SS precursors. Geophys. J. Int. 220, 1978–1994. doi:10.1093/gji/ggz546

Hao, S., Wang, W., Qian, W., Wu, Z., 2019. Elasticity of akimotoite under the mantle conditions: Implications for multiple discontinuities and seismic anisotropies at the depth of ~600–750 km in subduction zones. Earth Planet. Sci. Lett. 528, 115830. doi:10.1016/j.epsl.2019.115830

Hernández, E.R., Alfè, D., Brodholt, J., 2013. The incorporation of water into lower-mantle perovskites: A first-principles study. Earth Planet. Sci. Lett. 364, 37–43. doi:10.1016/j.epsl.2013.01.005

Higo, Y., Inoue, T., Irifune, T., Yurimoto, H., 2001. Effect of water on the spinel-postspinel transformation in Mg 2 SiO 4. Geophys. Res. Lett. 28, 3505–3508. doi:10.1029/2001GL013194

Hirose, K., 2002. Phase transitions in pyrolitic mantle around 670-km depth:

Implications for upwelling of plumes from the lower mantle. J. Geophys. Res. Solid Earth 107, ECV 3-1-ECV 3-13. doi:10.1029/2001JB000597

Houser, C., 2016. Global seismic data reveal little water in the mantle transition zone. Earth Planet. Sci. Lett. 448, 94–101. doi:10.1016/j.epsl.2016.04.018

Hu, Y., Wu, Z., Dera, P., Bina, C., 2016. Thermodynamic and elastic properties of pyrope at high pressure and high temperature by first-principles calculations. J. Geophys. Res. 1–15. doi:10.1002/2016JB013026.Received

Huang, X., Xu, Y., Karato, S., 2005. Water content in the transition zone from electrical conductivity of wadsleyite and ringwoodite. Nature 434, 746–749. doi:10.1038/nature03426

Inoue, T., Wada, T., Sasaki, R., Yurimoto, H., 2010. Water partitioning in the Earth's mantle. Phys. Earth Planet. Inter. 183, 245–251. doi:10.1016/j.pepi.2010.08.003

Inoue, T., Yurimoto, H., Kudoh, Y., 1995. Hydrous modified spinel, Mg 1.75 SiH 0.5 O 4 : A new water reservoir in the mantle transition region. Geophys. Res. Lett. 22, 117–120. doi:10.1029/94GL02965

Irifune, T., 1998. The Postspinel Phase Boundary in Mg2SiO4 Determined by in Situ X-ray Diffraction. Science (80-.). 279, 1698–1700. doi:10.1126/science.279.5357.1698

Irifune, T., Higo, Y., Inoue, T., Kono, Y., Ohfuji, H., Funakoshi, K., 2008. Sound velocities of majorite garnet and the composition of the mantle transition region. Nature 451, 814–817. doi:10.1038/nature06551

Irifune, T., Shinmei, T., McCammon, C.A., Miyajima, N., Rubie, D.C., Frost, D.J., 2010. Iron partitioning and density changes of pyrolite in Earth's lower mantle. Science (80-.). 327, 193–195. doi:10.1126/science.1181443

Jacobsen, S.D., Demouchy, S., Frost, D.J., Ballaran, T.B., Kung, J., 2005. A systematic study of OH in hydrous wadsleyite from polarized FTIR spectroscopy and single-crystal X-ray diffraction: Oxygen sites for hydrogen storage in Earth's interior. Am. Mineral. 90, 61–70. doi:10.2138/am.2005.1624

Jacobsen, S.D., Smyth, J.R., 2006. Effect of Water on the Sound Velocities of Ringwoodite in the Transition Zone, in: Geophysical Monograph Series. pp. 131–145. doi:10.1029/168GM10

Jacobsen, S.D., Smyth, J.R., Spetzler, H., Holl, C.M., Frost, D.J., 2004. Sound velocities and elastic constants of iron-bearing hydrous ringwoodite. Phys. Earth Planet. Inter. 143–144, 47–56. doi:10.1016/j.pepi.2003.07.019

Karato, S., 2011. Water distribution across the mantle transition zone and its implications for global material circulation. Earth Planet. Sci. Lett. 301, 413–423. doi:10.1016/j.epsl.2010.11.038

Kelbert, A., Schultz, A., Egbert, G., 2009. Global electromagnetic induction constraints on transition-zone water content variations. Nature 460, 1003–1006. doi:10.1038/nature08257

Li, J., Wang, Xin, Wang, Xiujiao, Yuen, D.A., 2013. P and SH velocity structure in the upper mantle beneath Northeast China: Evidence for a stagnant slab in hydrous mantle transition zone. Earth Planet. Sci. Lett. 367, 71–81. doi:10.1016/j.epsl.2013.02.026

Li, L., Brodholt, J., Alfè, D., 2009. Structure and elasticity of hydrous ringwoodite: A first principle investigation. Phys. Earth Planet. Inter. 177, 103–115. doi:10.1016/j.pepi.2009.07.007

Mao, Z., Lin, J.-F., Jacobsen, S.D., Duffy, T.S., Chang, Y.-Y., Smyth, J.R., Frost, D.J., Hauri, E.H., Prakapenka, V.B., 2012. Sound velocities of hydrous ringwoodite to 16GPa and 673K. Earth Planet. Sci. Lett. 331–332, 112–119. doi:10.1016/j.epsl.2012.03.001

Meier, U., Trampert, J., Curtis, A., 2009. Global variations of temperature and water content in the mantle transition zone from higher mode surface waves. Earth Planet. Sci. Lett. 282, 91–101. doi:10.1016/j.epsl.2009.03.004

Munch, F.D., Grayver, A. V., Guzavina, M., Kuvshinov, A. V., Khan, A., 2020. Joint Inversion of Daily and Long-Period Geomagnetic Transfer Functions Reveals Lateral Variations in Mantle Water Content. Geophys. Res. Lett. 47, 1–13. doi:10.1029/2020GL087222

Munch, F.D., Grayver, A. V., Kuvshinov, A., Khan, A., 2018. Stochastic Inversion of Geomagnetic Observatory Data Including Rigorous Treatment of the Ocean Induction Effect With Implications for Transition Zone Water Content and Thermal Structure. J. Geophys. Res. Solid Earth 123, 31–51. doi:10.1002/2017JB014691

Núñez-Valdez, M., Umemoto, K., Wentzcovitch, R.M., 2010. Fundamentals of elasticity of (Mg 1− x , Fe x) 2 SiO 4 olivine. Geophys. Res. Lett. 37, n/a-n/a. doi:10.1029/2010GL044205

Núñez-Valdez, M., Wu, Z., Yu, Y.G., Wentzcovitch, R.M., 2013. Thermal elasticity of (Fe x ,Mg 1− x) 2 SiO 4 olivine and wadsleyite. Geophys. Res. Lett. 40, 290–294. doi:10.1002/grl.50131

Núñez Valdez, M., Wu, Z., Yu, Y.G., Revenaugh, J., Wentzcovitch, R.M., 2012. Thermoelastic properties of ringwoodite (Fex,Mg1−x)2SiO4: Its relationship to the 520km seismic discontinuity. Earth Planet. Sci. Lett. 351–352, 115–122. doi:10.1016/j.epsl.2012.07.024

Ohtani, E., 2015. Hydrous minerals and the storage of water in the deep mantle. Chem. Geol. 418, 6–15. doi:10.1016/j.chemgeo.2015.05.005

Panero, W.R., 2010. First principles determination of the structure and elasticity of hydrous ringwoodite. J. Geophys. Res. 115, B03203. doi:10.1029/2008JB006282

Pearson, D.G., Brenker, F.E., Nestola, F., McNeill, J., Nasdala, L., Hutchison, M.T., Matveev, S., Mather, K., Silversmit, G., Schmitz, S., Vekemans, B., Vincze, L., 2014. Hydrous mantle transition zone indicated by ringwoodite included within diamond. Nature 507, 221–224. doi:10.1038/nature13080

Purevjav, N., Okuchi, T., Tomioka, N., Abe, J., Harjo, S., 2014. Hydrogen site analysis of hydrous ringwoodite in mantle transition zone by pulsed neutron diffraction. Geophys. Res. Lett. 41, 6718–6724. doi:10.1002/2014GL061448

Qian, W., Wang, W., Zou, F., Wu, Z., 2018. Elasticity of Orthoenstatite at High Pressure and Temperature: Implications for the Origin of Low V_P / V_S Zones in the Mantle Wedge. Geophys. Res. Lett. 45, 665–673. doi:10.1002/2017GL075647

Ritsema, J., Deuss, A., van Heijst, H.J., Woodhouse, J.H., 2011. S40RTS: a degree-40 shear-velocity model for the mantle from new Rayleigh wave dispersion, teleseismic traveltime and normal-mode splitting function measurements. Geophys. J. Int. 184, 1223–1236. doi:10.1111/j.1365-246X.2010.04884.x

Schmandt, B., Jacobsen, S.D., Becker, T.W., Liu, Z., Dueker, K.G., 2014. Dehydration melting at the top of the lower mantle. Science (80-.). 344, 1265–1268. doi:10.1126/science.1253358

Schulze, K., Marquardt, H., Kawazoe, T., Boffa Ballaran, T., McCammon, C., Koch-Müller, M., Kurnosov, A., Marquardt, K., 2018. Seismically invisible water in Earth's transition zone? Earth Planet. Sci. Lett. 498, 9–16. doi:10.1016/j.epsl.2018.06.021

Semenov, A., Kuvshinov, A., 2012. Global 3-D imaging of mantle conductivity based on inversion of observatory C -responses-II. Data analysis and results. Geophys. J. Int. 191, no-no. doi:10.1111/j.1365-246X.2012.05665.x

Shimizu, H., Utada, H., Baba, K., Koyama, T., Obayashi, M., Fukao, Y., 2010. Three-dimensional imaging of electrical conductivity in the mantle transition zone beneath the North Pacific Ocean by a semi-global induction study. Phys. Earth Planet. Inter. 183, 252–269. doi:10.1016/j.pepi.2010.01.010

Shukla, G., Cococcioni, M., Wentzcovitch, R.M., 2016. Thermoelasticity of Fe^{3+} - and Al-bearing bridgmanite. Geophys. Res. Lett. doi:10.1002/2016GL069332

Shukla, G., Wu, Z., Hsu, H., Floris, A., Cococcioni, M., Wentzcovitch, R.M., 2015. Thermoelasticity of Fe^{2+} -bearing bridgmanite. Geophys. Res. Lett. 42, 1741–1749. doi:10.1002/2014GL062888

Smyth, J.R., 1987. The beta -Mg_2SiO_4: a potential host for water in the mantle? Am. Mineral. 72, 1051–1055. doi:0003-{04x/87ll l 12-1051$02

Suetsugu, D., Inoue, T., Yamada, A., Zhao, D., Obayashi, M., 2006. Towards mapping the three-dimensional distribution of water in the transition zone from P-velocity tomography and 660-km discontinuity depths, in: Earth's Deep Water Cycle. pp. 237–249. doi:10.1029/168GM18

Tang, Y., Obayashi, M., Niu, F., Grand, S.P., Chen, Y.J., Kawakatsu, H., Tanaka, S., Ning, J., Ni, J.F., 2014. Changbaishan volcanism in northeast China linked to subduction-induced mantle upwelling. Nat. Geosci. 7, 470–475. doi:10.1038/ngeo2166

Tauzin, B., Debayle, E., Wittlinger, G., 2010. Seismic evidence for a global low-velocity layer within the Earth's upper mantle. Nat. Geosci. 3, 718–721. doi:10.1038/ngeo969

Thio, V., Cobden, L., Trampert, J., 2016. Seismic signature of a hydrous mantle transition zone. Phys. Earth Planet. Inter. 250, 46–63.

doi:10.1016/j.pepi.2015.11.005

Thomas, S., Jacobsen, S.D., Bina, C.R., Reichart, P., Moser, M., Hauri, E.H., Koch-MÃ¼ller, M., Smyth, J.R., Dollinger, G., 2015. Quantification of water in hydrous ringwoodite. Front. Earth Sci. 2, 1–10. doi:10.3389/feart.2014.00038

Tschauner, O., Huang, S., Greenberg, E., Prakapenka, V.B., Ma, C., Rossman, G.R., Shen, A.H., Zhang, D., Newville, M., Lanzirotti, A., Tait, K., 2018. Ice-VII inclusions in diamonds: Evidence for aqueous fluid in Earth's deep mantle. Science (80-.). 359, 1136–1139. doi:10.1126/science.aao3030

Wang, F., Barklage, M., Lou, X., van der Lee, S., Bina, C.R., Jacobsen, S.D., 2018. HyMaTZ: A Python Program for Modeling Seismic Velocities in Hydrous Regions of the Mantle Transition Zone. Geochemistry, Geophys. Geosystems 19, 2308–2324. doi:10.1029/2018GC007464

Wang, J., Sinogeikin, S. V., Inoue, T., Bass, J.D., 2006. Elastic properties of hydrous ringwoodite at high-pressure conditions. Geophys. Res. Lett. 33, L14308. doi:10.1029/2006GL026441

Wang, W., Walter, M.J., Peng, Y., Redfern, S., Wu, Z., 2019. Constraining olivine abundance and water content of the mantle at the 410-km discontinuity from the elasticity of olivine and wadsleyite. Earth Planet. Sci. Lett. 519, 1–11. doi:10.1016/j.epsl.2019.04.018

Wang, W., Wu, Z., 2018. Elasticity of Corundum at High Pressures and Temperatures: Implications for Pyrope Decomposition and Al-Content Effect on Elastic Properties of Bridgmanite. J. Geophys. Res. Solid Earth 123, 1201–1216. doi:10.1002/2017JB015088

Wang, W., Xu, Y., Sun, D., Ni, S., Wentzcovitch, R., Wu, Z., 2020. Velocity and density characteristics of subducted oceanic crust and the origin of lower-mantle heterogeneities. Nat. Commun. 11, 64. doi:10.1038/s41467-019-13720-2

Wei, S.S., Shearer, P.M., 2017. A sporadic low-velocity layer atop the 410 km discontinuity beneath the Pacific Ocean. J. Geophys. Res. Solid Earth 122, 5144–5159. doi:10.1002/2017JB014100

Wentzcovitch, R.M., 1991. Invariant molecular-dynamics approach to structural phase transitions. Phys. Rev. B 44, 2358–2361. doi:10.1103/PhysRevB.44.2358

Wood, B.J., 1995. The Effect of H2O on the 410-Kilometer Seismic Discontinuity. Science (80-.). 268, 74–76. doi:10.1126/science.268.5207.74

Wu, Z., Huang, F., Huang, S., 2015. Isotope fractionation induced by phase transformation: First-principles investigation for Mg2SiO4. Earth Planet. Sci. Lett. 409, 339–347. doi:10.1016/j.epsl.2014.11.004

Wu, Z., Justo, J.F., Wentzcovitch, R.M., 2013. Elastic Anomalies in a Spin-Crossover System: Ferropericlase at Lower Mantle Conditions. Phys. Rev. Lett. 110, 228501. doi:10.1103/PhysRevLett.110.228501

Wu, Z., Wang, W., 2016. First-principles calculations of elasticity of minerals at high temperature and pressure. Sci. China Earth Sci. 59, 1107–1137. doi:10.1007/s11430-016-5296-6

Wu, Z., Wentzcovitch, R.M., 2011. Quasiharmonic thermal elasticity of crystals: An analytical approach. Phys. Rev. B 83, 184115. doi:10.1103/PhysRevB.83.184115

Yang, D., Wang, W., Wu, Z., 2017. Elasticity of superhydrous phase B at the mantle temperatures and pressures: Implications for 800 km discontinuity and water flow into the lower mantle. J. Geophys. Res. Solid Earth 122, 5026–5037. doi:10.1002/2017JB014319

Yang, R., Wu, Z., 2014. Elastic properties of stishovite and the CaCl 2 -type silica at the mantle temperature and pressure: An ab initio investigation. Earth Planet. Sci. Lett. 404, 14–21. doi:10.1016/j.epsl.2014.07.020

Ye, Y., Brown, D.A., Smyth, J.R., Panero, W.R., Jacobsen, S.D., Chang, Y.-Y., Townsend, J.P., Thomas, S.-M., Hauri, E.H., Dera, P., Frost, D.J., 2012. Compressibility and thermal expansion of hydrous ringwoodite with 2.5(3) wt% H2O. Am. Mineral. 97, 573–582. doi:10.2138/am.2012.4010

Yoshino, T., Manthilake, G., Matsuzaki, T., Katsura, T., 2008. Dry mantle transition zone inferred from the conductivity of wadsleyite and ringwoodite. Nature 451, 326–329. doi:10.1038/nature06427

Yu, Y.G., Wentzcovitch, R.M., Tsuchiya, T., Umemoto, K., Weidner, D.J., 2007. First principles investigation of the postspinel transition in Mg 2 SiO 4. Geophys. Res. Lett. 34, L10306. doi:10.1029/2007GL029462

Zou, F., Wu, Z., Wang, W., Wentzcovitch, R.M., 2018. An Extended Semianalytical Approach for Thermoelasticity of Monoclinic Crystals: Application to Diopside. J. Geophys. Res. Solid Earth 123, 7629–7643. doi:10.1029/2018JB016102

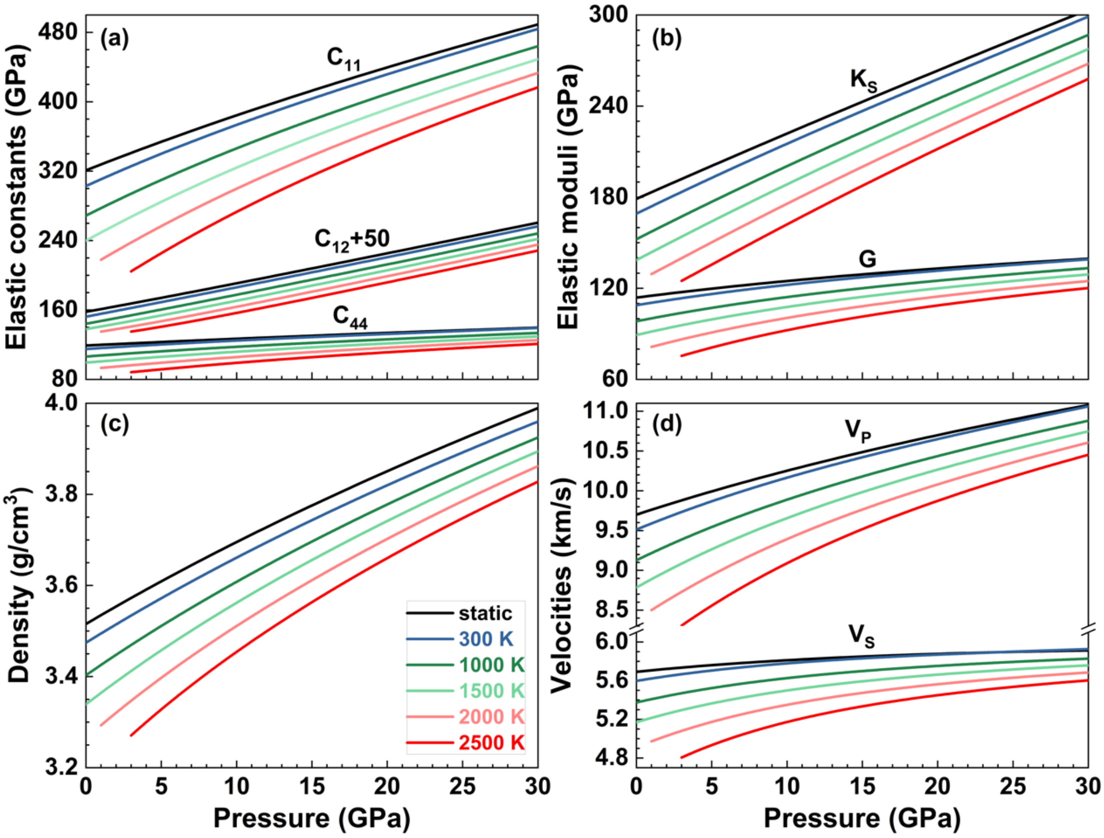

Figure 1. Elastic moduli, density, and velocities of hydrous ringwoodite with 1.63 wt% H_2O ($Mg_{15}H_2Si_8O_{32}$) at different pressures and temperatures. (a) elastic constants (C_{11}, C_{12}, and C_{44}), (b) bulk and shear moduli (K_S and G), (c) density, and (d) compressional and shear wave velocities (V_P and V_S).

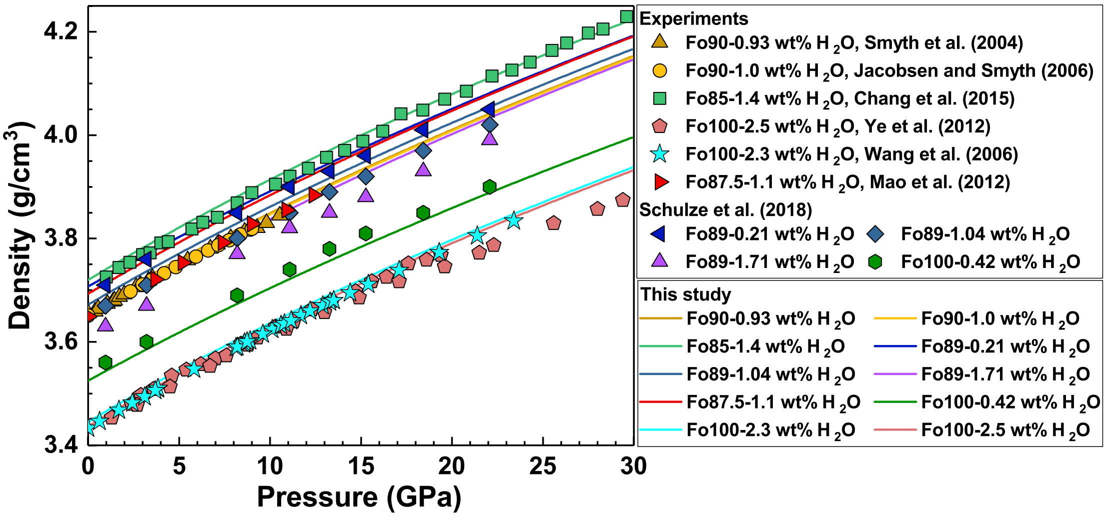

Figure 2. Comparisons of the density of hydrous ringwoodite between theoretical results and experimental measurements (Chang et al., 2015; Jacobsen et al., 2004; Jacobsen and Smyth, 2006; Mao et al., 2012; Schulze et al., 2018; Wang et al., 2006; Ye et al., 2012) (scattered points). Solid lines represent the density of hydrous ringwoodite with different water and Fe contents using linear interpolation from calculated results of $Mg_{15}Si_8O_{30}(OH)_2$ ringwoodite in this study and anhydrous ringwoodite (Fo100 and Fo87.5) in previous work (Núñez Valdez et al., 2012). The Fe content of ringwoodite is marked by the Mg_2SiO_4 fraction (Fo). The combined effect is estimated by adding the water and Fe effects together.

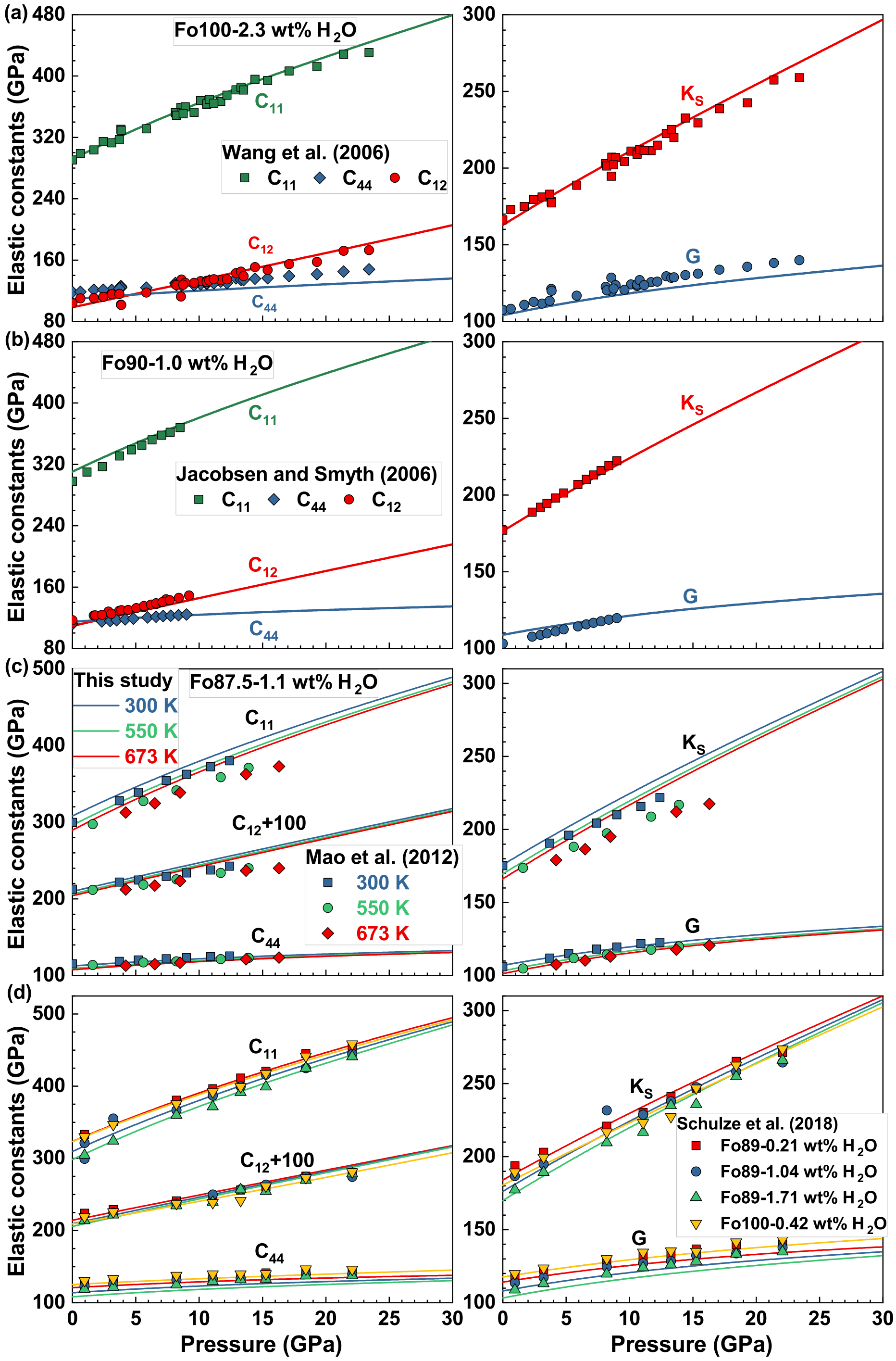

Figure 3. Comparisons of the elastic properties of hydrous ringwoodite between theoretical results and experimental measurements (Jacobsen and Smyth, 2006; Mao et al., 2012; Schulze et al., 2018; Wang et al., 2006) (scattered points). Solid lines represent the theoretical results estimated using linear interpolation from calculated results of $Mg_{15}Si_8O_{30}(OH)_2$ ringwoodite in this study and anhydrous ringwoodite (Fo100 and Fo87.5) in previous work (Núñez Valdez et al., 2012).

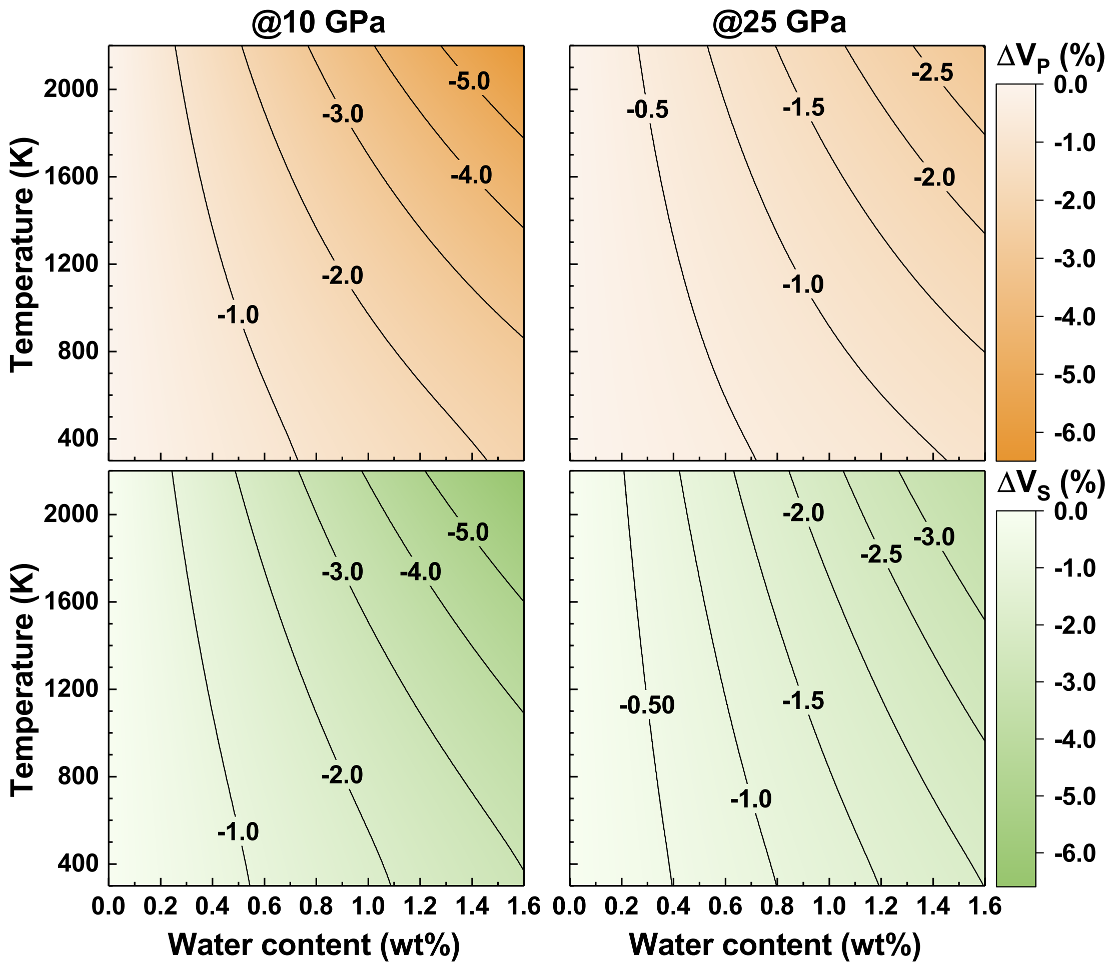

Figure 4. Velocity reductions in ringwoodite as a function of water content at different temperatures and pressures (10 GPa and 25 GPa). The velocity contrasts (ΔV_P and ΔV_S) refer to the V_P and V_S differences between hydrous and anhydrous ringwoodite.

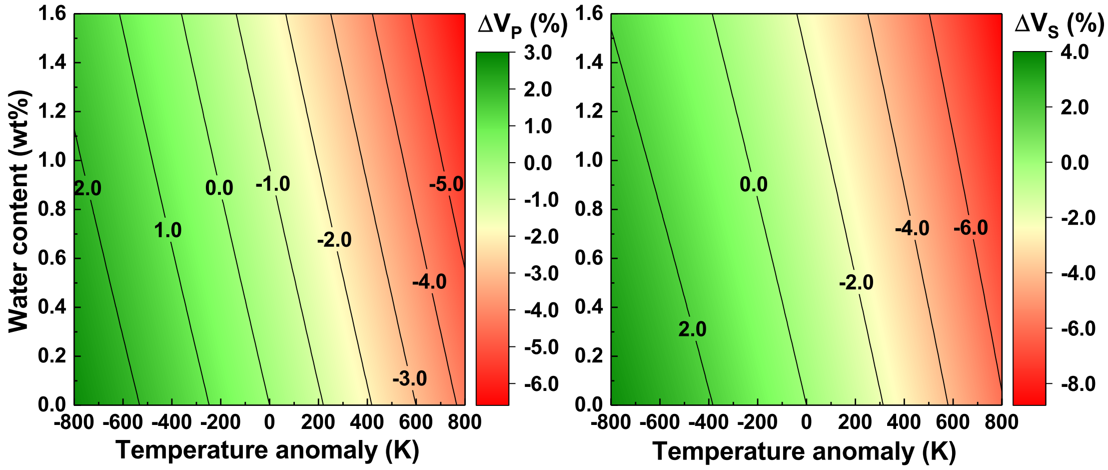

Figure 5. Velocity anomalies (ΔV_P and ΔV_S) in pyrolite caused by ringwoodite hydration and temperature anomaly at 23.5 GPa. Under the conditions of the MTZ, pyrolite consists of ~ 57% ringwoodite, 35% majorite, and 8% calcium perovskite (Irifune et al., 2010). The velocities of anhydrous pyrolite are taken as the references to calculate ΔV_P and ΔV_S. The temperature anomaly is with respect to the normal mantle temperature from Brown and Shankland (1981).

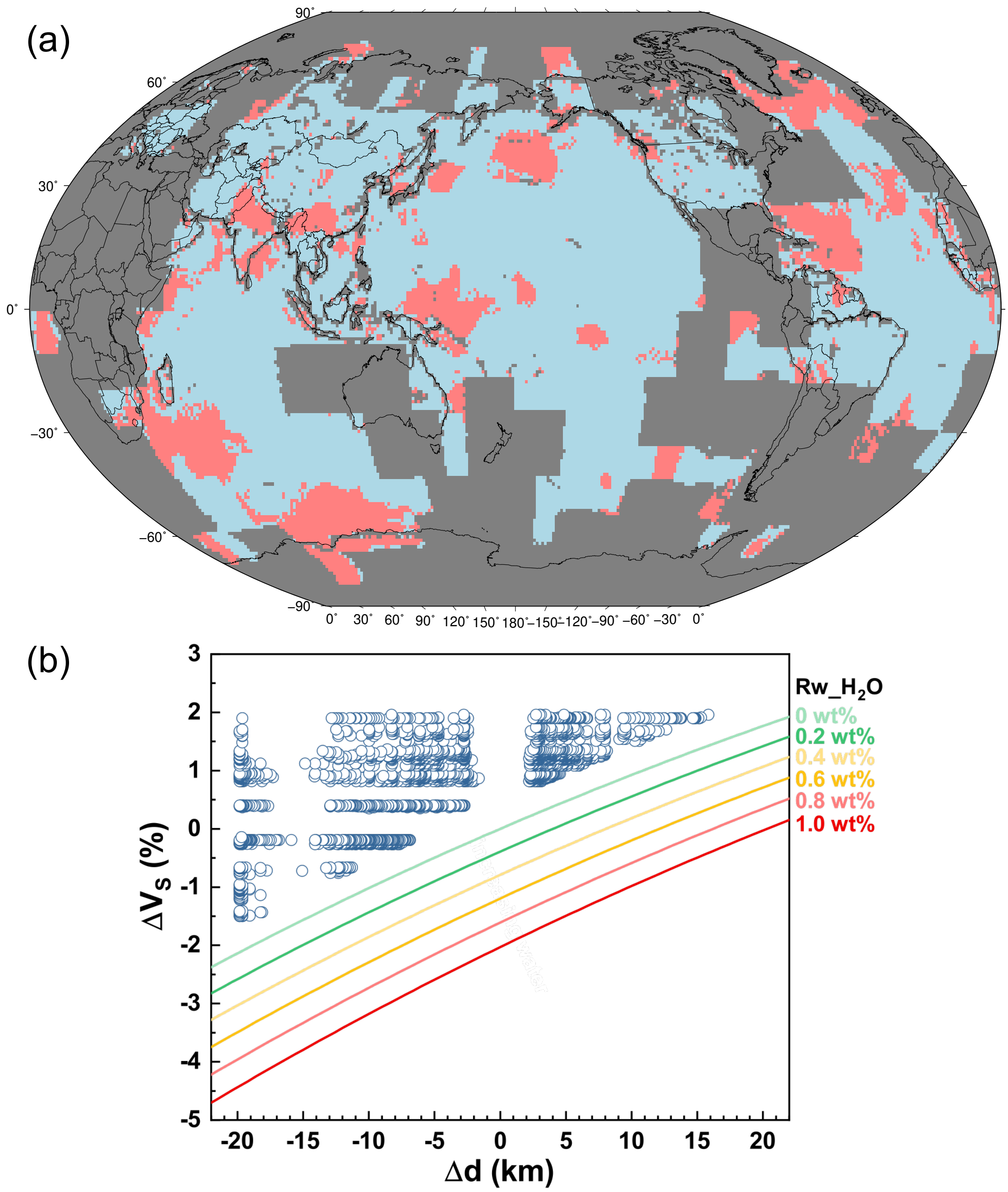

Figure 6. (a) Regions covered by the seismic observations (the depth variation of 660-km discontinuity (Δd) and the shear velocity anomaly (ΔV_S)). The blue areas (79%) represent the bins with Δd and ΔV_S that can be matched by our models and the red areas (21%) are the remaining bins that are not consistent with the current mineral models. (b) the ΔV_S and Δd within the remaining 21% of bins (open circles) compared to the predictions from mineral physics (lines). Rw_H_2O refers to the water concentration in ringwoodite.

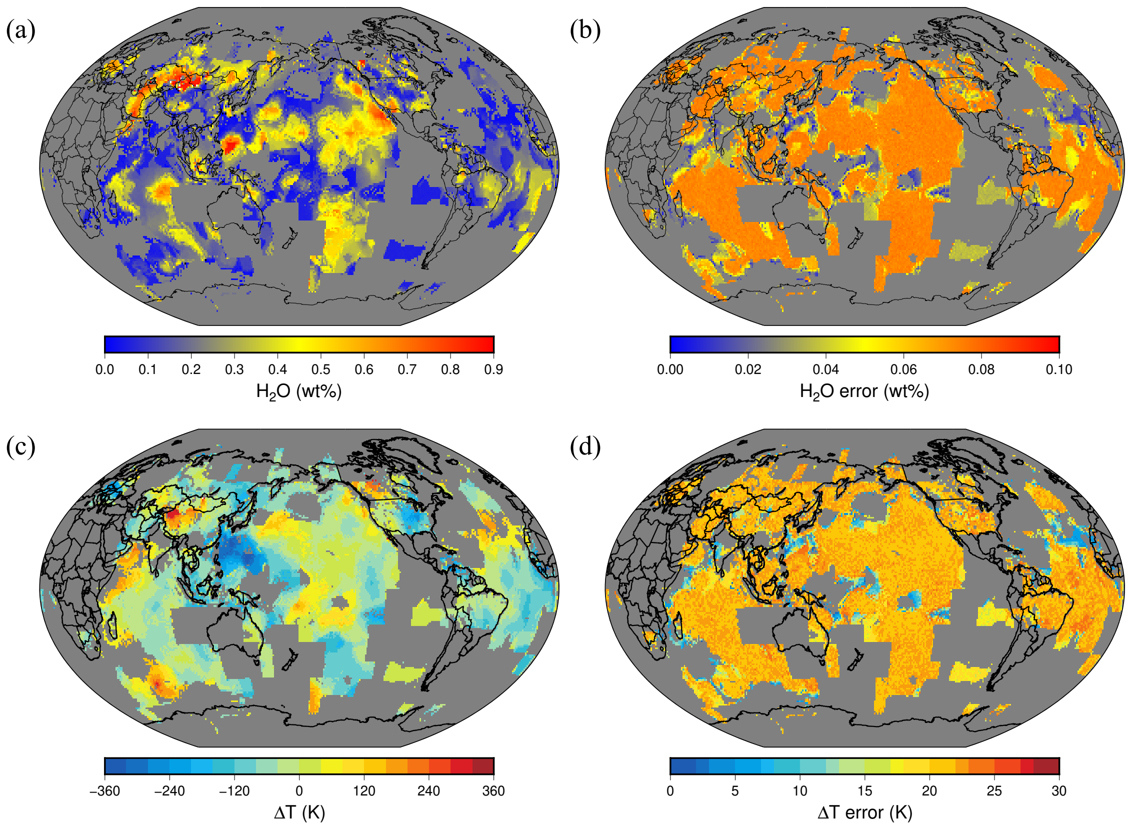

Figure 7. Water concentration (H_2O wt%) and temperature anomaly (ΔT (K)) in the lower MTZ inferred from the depth variation of 660-km discontinuity and the shear velocity anomaly. (a) the map of water concentration and (b) the standard error of H_2O amount; (c) the map of temperature anomaly and (d) the standard error of ΔT.

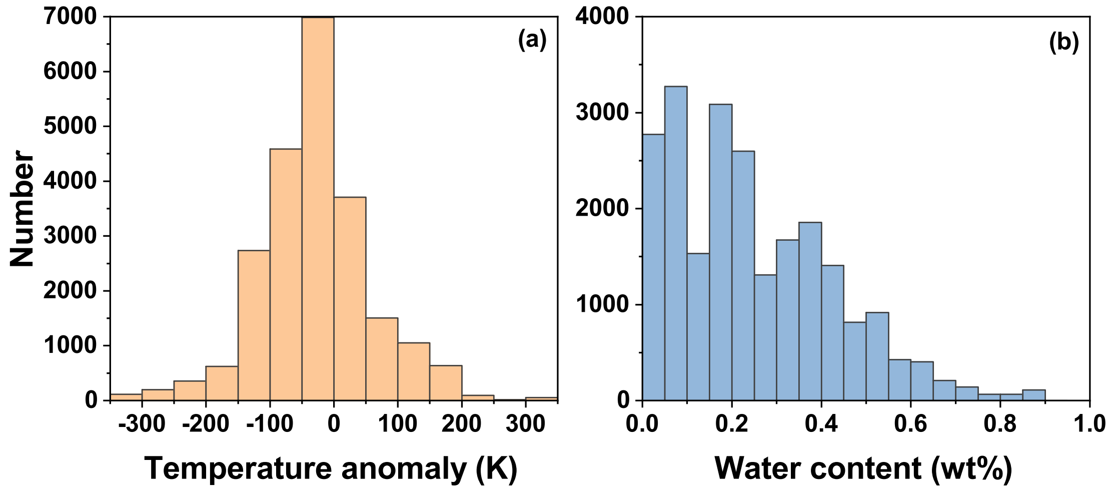

Figure 8. Distributions of temperature anomaly and water content from each bin with the observed ΔV_S and Δd that are consistent with the mineral physics model. The average temperature anomaly and water concentration are -29±21 K and 0.25±0.06 wt%, respectively.

Table S1. Density, elastic moduli, and sound velocities of hydrous ringwoodite with different substitution mechanisms at static conditions.

Substitutions	Pressure (GPa)	density (g/cm^3)	K_S (GPa)	G (GPa)	V_P (km/s)	V_S (km/s)
Mechanism 1 $Mg_{15}H_2Si_8O_{32}$ V_{Mg}'' +2H** 1.63 wt% H_2O	0	3.536	183.9	115.1	9.767	5.705
	5	3.628	205.5	121.1	10.057	5.777
	10	3.713	226.6	126.3	10.313	5.831
	15	3.793	247.0	130.2	10.530	5.859
	20	3.867	267.7	132.8	10.724	5.860
	30	4.004	308.5	140.6	11.130	5.926
Mechanism 2 $Mg_{32}Si_{15}H_4O_{64}$ V_{Si}'''' +4H**** 1.62 wt% H_2O	0	3.539	179.2	110.6	9.607	5.590
	5	3.632	202.2	121.7	10.016	5.788
	10	3.719	223.7	127.9	10.297	5.865
	15	3.799	246.0	133.0	10.556	5.916
	20	3.874	266.1	137.3	10.768	5.953
	30	4.011	306.8	143.8	11.148	5.987
Mechanism 3 $Mg_{16}H_2Si_7O_{32}$ Mg_{Si}'' +2H** 1.64 wt% H_2O	0	3.418	178.3	109.4	9.738	5.657
	5	3.509	200.0	115.3	10.040	5.732
	10	3.593	221.5	119.8	10.301	5.774
	15	3.671	241.9	123.7	10.528	5.806
	20	3.744	261.9	126.7	10.727	5.817
	30	3.879	300.3	131.3	11.069	5.818
*(1):(2):(3)=65:25:10 1.63 wt% H_2O	0	3.525	182.1	113.4	9.724	5.672
	5	3.617	204.1	120.7	10.045	5.775
	10	3.703	225.4	126.0	10.308	5.834
	15	3.782	246.2	130.2	10.536	5.868
	20	3.857	266.7	133.3	10.735	5.879
	30	3.993	307.3	140.5	11.128	5.930

**(1):(2):(3)=75:14:11 1.63 wt% H_2O	0	3.524	182.6	113.8	9.741	5.684
	5	3.616	204.4	120.5	10.049	5.773
	10	3.701	225.7	125.8	10.310	5.830
	15	3.780	246.3	129.9	10.534	5.861
	20	3.855	266.8	132.8	10.731	5.868
	30	3.991	307.4	140.0	11.126	5.923

There are three possible mechanisms for the incorporation of hydrogen into ringwoodite (Panero, 2010): (1) V_{Mg}'' +2H**, Mg vacancy with charge balanced by two H atoms; (2) V_{Si}'''' +4H****, Si vacancy with charge balanced by four H atoms; (3) Mg_{Si}'' +2H**, Si vacancy is occupied by Mg atom with charge balanced by two H atoms. Previous first-principles calculations (Panero, 2010) found that the three substitution mechanisms exist in ratios of 64:25:10 for (1):(2):(3). Results of a least squares fit to existing experimental data on hydrous ringwoodite show the three defects in ratios of 75:14:11 (Panero, 2010).

*Results of hydrous ringwoodite with the substitution mechanism ratios of 65:25:10.

**Results of hydrous ringwoodite with the substitution mechanism ratios of 75:14:11.

Table S2. The water effects on the elastic moduli, density, and sound velocities of ringwoodite calculated within LDA and GGA at static conditions.

	P (GPa)	GGA					LDA				
		K_S (GPa)	G (GPa)	V_P (km/s)	V_S (km/s)	density (g/cm^3)	K_S (GPa)	G (GPa)	V_P (km/s)	V_S (km/s)	density (g/cm^3)
Anhydrous ringwoodite (Mg_2SiO_4)	0	176.3	118.6	9.791	5.831	3.490	196.3	124.6	10.018	5.874	3.611
	5	197.8	125.4	10.091	5.915	3.584	217.4	130.9	10.293	5.949	3.700
	10	218.6	131.3	10.356	5.981	3.671	238.3	135.3	10.523	5.982	3.782
	15	237.6	136.4	10.574	6.030	3.752	257.7	139.2	10.719	6.007	3.858
	20	257.8	140.8	10.789	6.066	3.828	278.5	142.8	10.920	6.026	3.932
	25	277.3	144.8	10.983	6.093	3.900	298.1	145.4	11.084	6.028	4.000
Hydrous ringwoodite ($Mg_{15}H_2Si_8O_{32}$)	0	163.1	107.8	9.487	5.623	3.408	183.9	115.1	9.767	5.705	3.536
	5	184.4	115.1	9.815	5.730	3.508	205.5	121.1	10.057	5.777	3.628
	10	205.4	121.2	10.100	5.804	3.599	226.6	126.3	10.313	5.831	3.713
	15	226.3	126.6	10.358	5.864	3.683	247.0	130.2	10.530	5.859	3.793
	20	246.5	131.6	10.590	5.913	3.762	267.7	132.8	10.724	5.860	3.867
	25	266.8	135.9	10.806	5.951	3.836	288.0	136.2	10.918	5.880	3.938
Reductions per weight of water	0	-8.1	-6.7	-0.186	-0.127	-0.050	-7.6	-5.8	-0.154	-0.103	-0.046
	5	-8.2	-6.3	-0.170	-0.114	-0.047	-7.3	-6.0	-0.145	-0.105	-0.044
	10	-8.0	-6.2	-0.157	-0.109	-0.044	-7.2	-5.6	-0.128	-0.093	-0.042
	15	-6.9	-6.0	-0.132	-0.102	-0.042	-6.6	-5.6	-0.116	-0.091	-0.040
	20	-6.9	-5.7	-0.122	-0.093	-0.040	-6.6	-6.1	-0.120	-0.102	-0.040
	25	-6.5	-5.5	-0.109	-0.087	-0.039	-6.2	-5.6	-0.101	-0.091	-0.038

Table S3. Elastic moduli and velocities of hydrous ringwoodite with 1.63 wt% H_2O ($Mg_{15}H_2Si_8O_{32}$) and their first and second derivatives with respect to pressure and temperature. The polynomial fitting equation is $M = M_0 + (\frac{\partial M}{\partial P}) \cdot P + (\frac{\partial M}{\partial T}) \cdot (T - 300) + (\frac{\partial^2 M}{\partial P^2}) \cdot P^2 + (\frac{\partial^2 M}{\partial T^2}) \cdot (T - 300)^2 + (\frac{\partial^2 M}{\partial P \partial T}) \cdot P \cdot (T - 300), M = C_{11}, C_{12}, C_{44}, K_S, G, V_P, and\ V_S.$

Parameters	C_{11}	C_{12}	C_{44}	K_S	G
$M_0\ (GPa)$	304.3	102.9	115.3	170.0	109.2
$\frac{\partial M}{\partial P}$	7.60	3.28	1.06	4.72	1.53
$\frac{\partial M}{\partial T}\ (MPa/K)$	-47.5	-12.4	-12.2	-24.1	-14.5
$\frac{\partial^2 M}{\partial P^2}\ (\times 10^{-3}\ GPa^{-1})$	-58.4	6.3	-9.9	-15.3	-19.9
$\frac{\partial^2 M}{\partial P \partial T}\ (\times 10^{-3}\ K^{-1})$	0.856	0.023	0.189	0.301	0.291
$\frac{\partial^2 M}{\partial T^2}\ (\times 10^{-6}\ GPa\ K^{-1})$	-3.09	-0.59	-0.62	-1.43	-0.90
	V_P			V_S	
$M_0\ (km\ s^{-1})$	9.526			5.603	
$\frac{\partial M}{\partial P}\ (km\ s^{-1}\ GPa^{-1})$	0.0735			0.0231	
$\frac{\partial M}{\partial T}\ (\times 10^{-3}\ km\ s^{-1}\ K^{-1})$	-0.523			-0.297	
$\frac{\partial^2 M}{\partial P^2}\ (\times 10^{-3}\ km\ s^{-1}\ GPa^{-2})$	-0.828			-0.471	
$\frac{\partial^2 M}{\partial P \partial T}\ (\times 10^{-6}\ km\ s^{-1}\ GPa^{-1} K^{-1})$	12.4			7.7	
$\frac{\partial^2 M}{\partial T^2}\ (\times 10^{-6}\ km\ s^{-1}\ K^{-2})$	0.041			-0.025	

Table S4. Equation of state of hydrous ringwoodite 1.63 wt% H_2O ($Mg_{15}H_2Si_8O_{32}$). The relationship between pressure and volume is fitted by the third-order Birch-Murnaghan equation: $P(V) = 3K_{T0}f(1+2f)^{5/2}(1+3/2(K'_{T0}-4)f)$, where $f = 1/2[(V_0/V)^{2/3}-1]$, P is pressure, V_0 is the volume at ambient pressure, V is high-pressure volume, and K_{T0} and K'_{T0} are the isothermal bulk modulus and its pressure derivative.

Temperature (K)	Pressure range (GPa)	V_0 (Å^3)	K_{T0} (GPa)	K'_{T0}
300	0-30	527.408	169.0	4.64
1000	0-30	538.459	148.0	4.91
1500	2-30	548.745	131.0	5.17
2000	3-40	561.258	112.6	5.50
2500	4-30	577.102	92.5	5.94

Table S5. Sound velocities of hydrous ringwoodite in Schulze et al. (2018) as a function of pressure and water content at 300 K. The polynomial fitting equation is: $V_{P/S} = p00 + p10 \cdot C_{H2O} + p01 \cdot P + p11 \cdot P \cdot C_{H2O} + p02 \cdot P^2$, where p00, p10, p01, p11, and p02 are polynomial fitting parameters (with 95% confidence bounds), C_{H2O} is water content, and P is pressure.

Parameters	V_P (km/s)	V_S (km/s)
p00	9.718±0.070	5.662±0.034
p10	-0.1955±0.0538	-0.1164±0.0256
p01	0.05807±0.00978	0.02081±0.00465
p11	0.006849±0.004019	0.002982±0.001909
p02 ($\times 10^{-3}$)	-0.6953±0.3837	-0.4406±0.1824

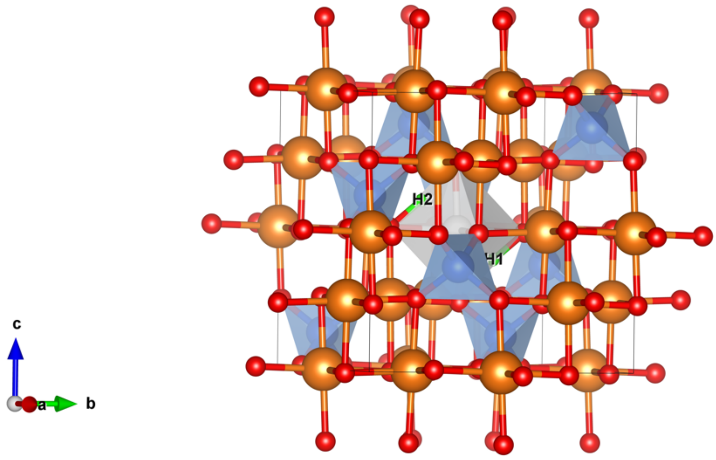

Figure S1. The relaxed structure of hydrous ringwoodite with 1.63 wt% water ($Mg_{15}Si_8O_{30}(OH)_2$). The initial configure was generated through the substitution mechanism V_{Mg}'' +2H**, which is the main mechanism for the incorporation of hydrogen into ringwoodite (Grüninger et al., 2017; Panero, 2010). The sites occupied by H atoms are derived from the experimental results of pulsed neutron diffraction (Purevjav et al., 2014).

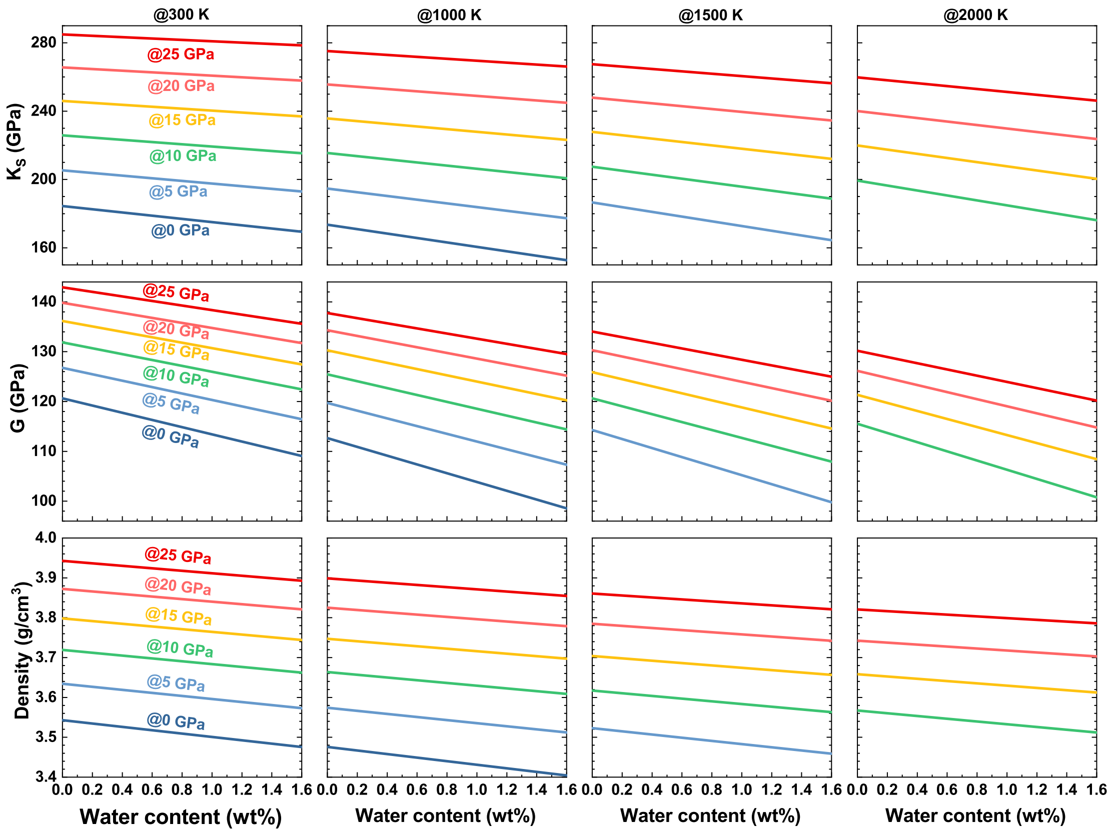

Figure S2. Elastic moduli (K_S and G) and density of ringwoodite as a function of water content at different pressures (0 GPa, 5 GPa, 10 GPa, 15 GPa, 20 GPa, and 25 GPa) and temperatures (300 K, 1000 K, 1500 K, and 2000 K). The elasticity of anhydrous ringwoodite is derived from Núñez Valdez et al. (2012).

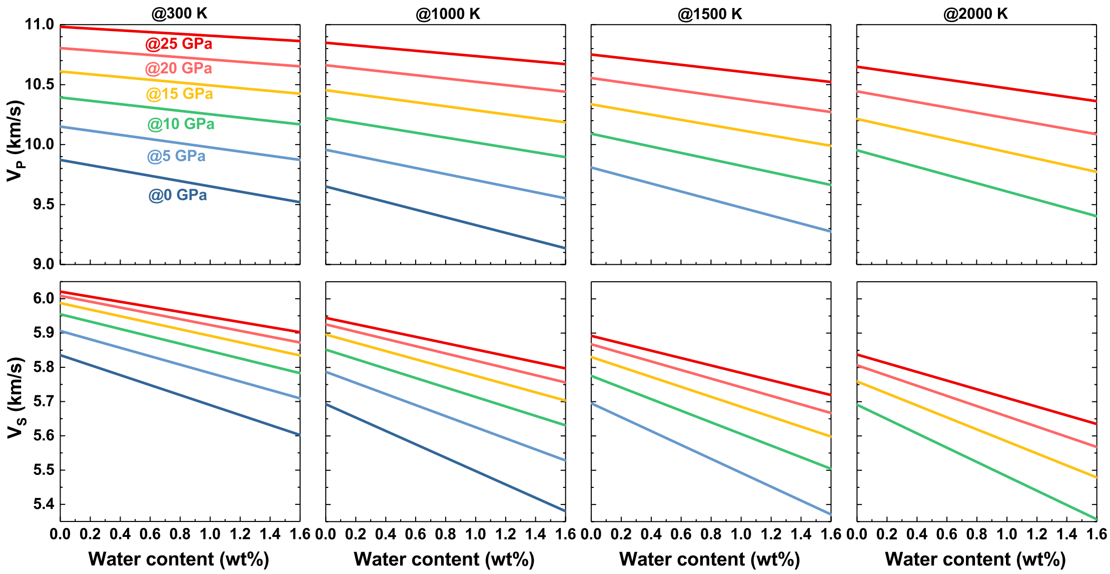

Figure S3. Compressional and shear wave velocities (V_P and V_S) of ringwoodite as a function of water content at different pressures (0 GPa, 5 GPa, 10 GPa, 15 GPa, 20 GPa, and 25 GPa) and temperatures (300 K, 1000 K, 1500 K, and 2000 K).

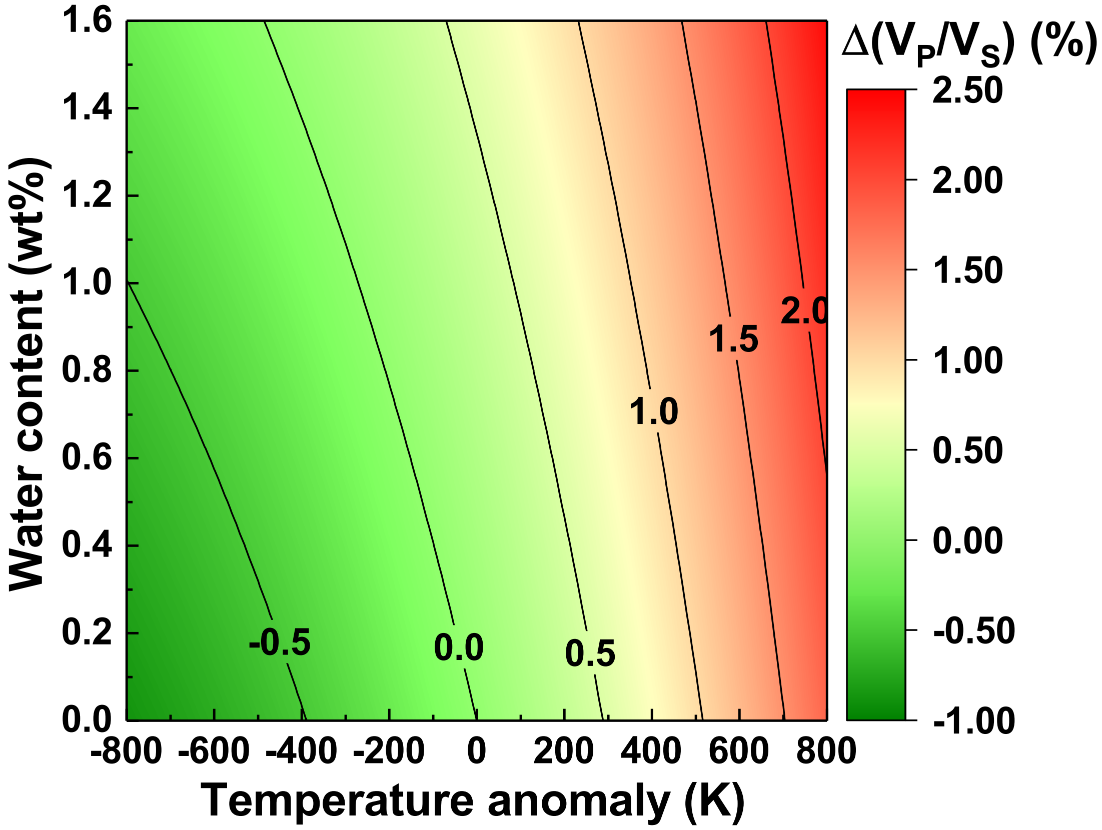

Figure S4. V_P/V_S anomalies ($\Delta(V_P/V_S)$) in pyrolite caused by ringwoodite hydration and temperature anomaly at 23.5 GPa. Under the conditions of the MTZ, pyrolite consists of ~ 57% ringwoodite, 35% majorite, and 8% calcium perovskite (Irifune et al., 2010). The V_P/V_S of anhydrous pyrolite is taken as the reference to calculate $\Delta(V_P/V_S)$. The temperature anomaly is with respect to the normal mantle temperature from Brown and Shankland (1981).

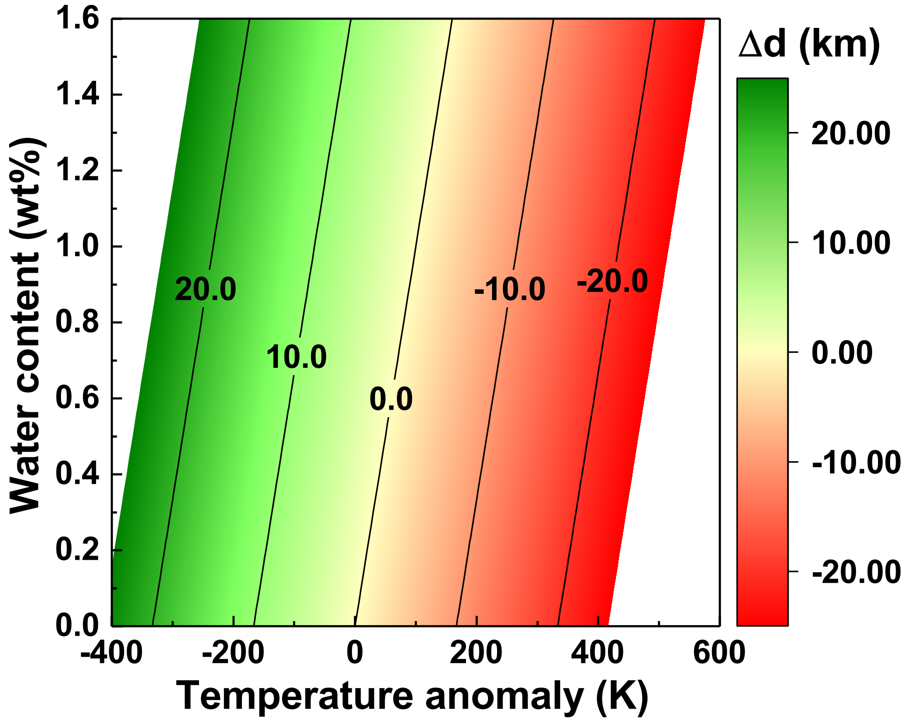

Figure S5. Depth variations in the 660-km discontinuity as a function of ringwoodite hydration and temperature anomaly. The effect of temperature on the depth of the 660-km discontinuity (-0.06 km/K) is derived from the Clapeyron slope of the post-spinel phase transition (Bina and Helffrich, 1994; Fei et al., 2004; Higo et al., 2001; Irifune, 1998; Yu et al., 2007). The effect of ringwoodite hydration on the depth of the 660-km discontinuity is adopted as 6 km/wt% (Higo et al., 2001).

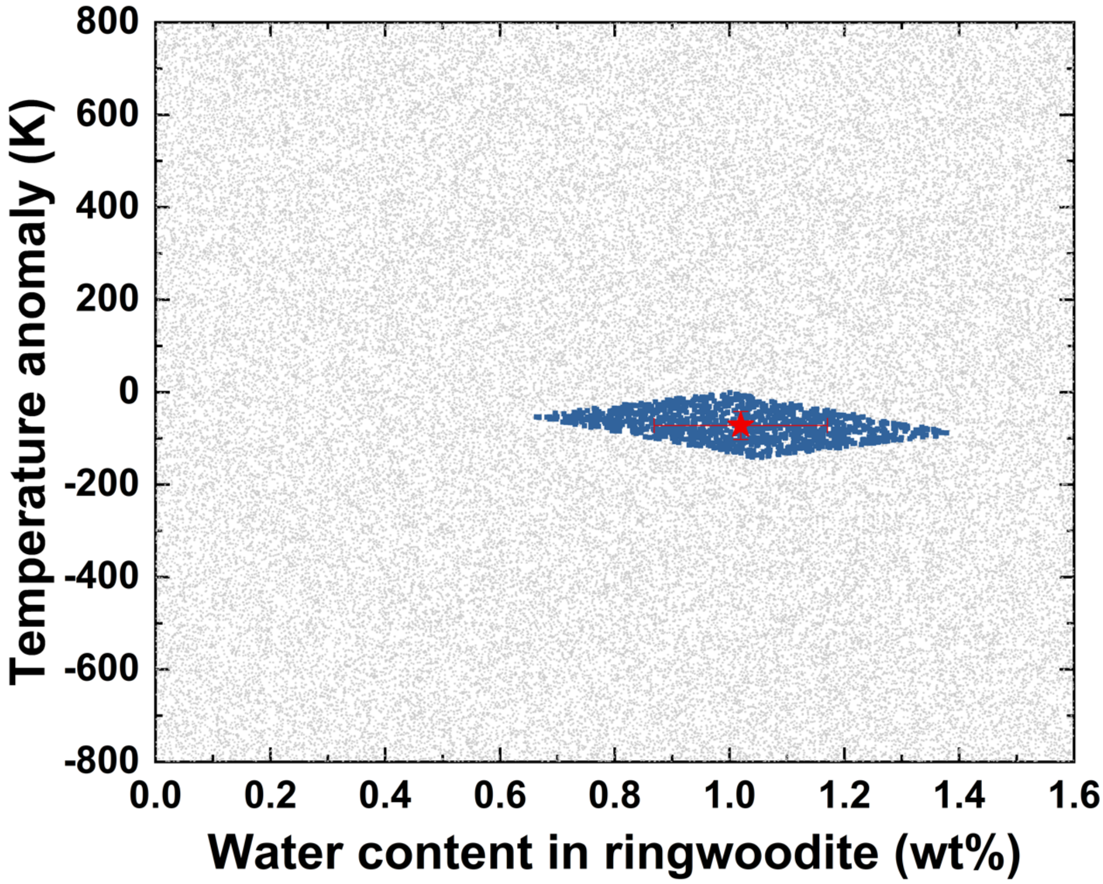

Figure S6. An example of Monte Carlo simulations to find out the solutions for water content in ringwoodite and temperature anomaly. The observed ΔV_S and Δd values are -1.0% and 9 km, respectively. 70000 initial inputs (grey points) were randomly produced in the ranges of 0-1.6 wt% for water content in ringwoodite and -800-+800 K for temperature anomaly. Blue points are the results that can match the observed ΔV_S within 0.3% and Δd within 3 km, and the red star refers to the average value.

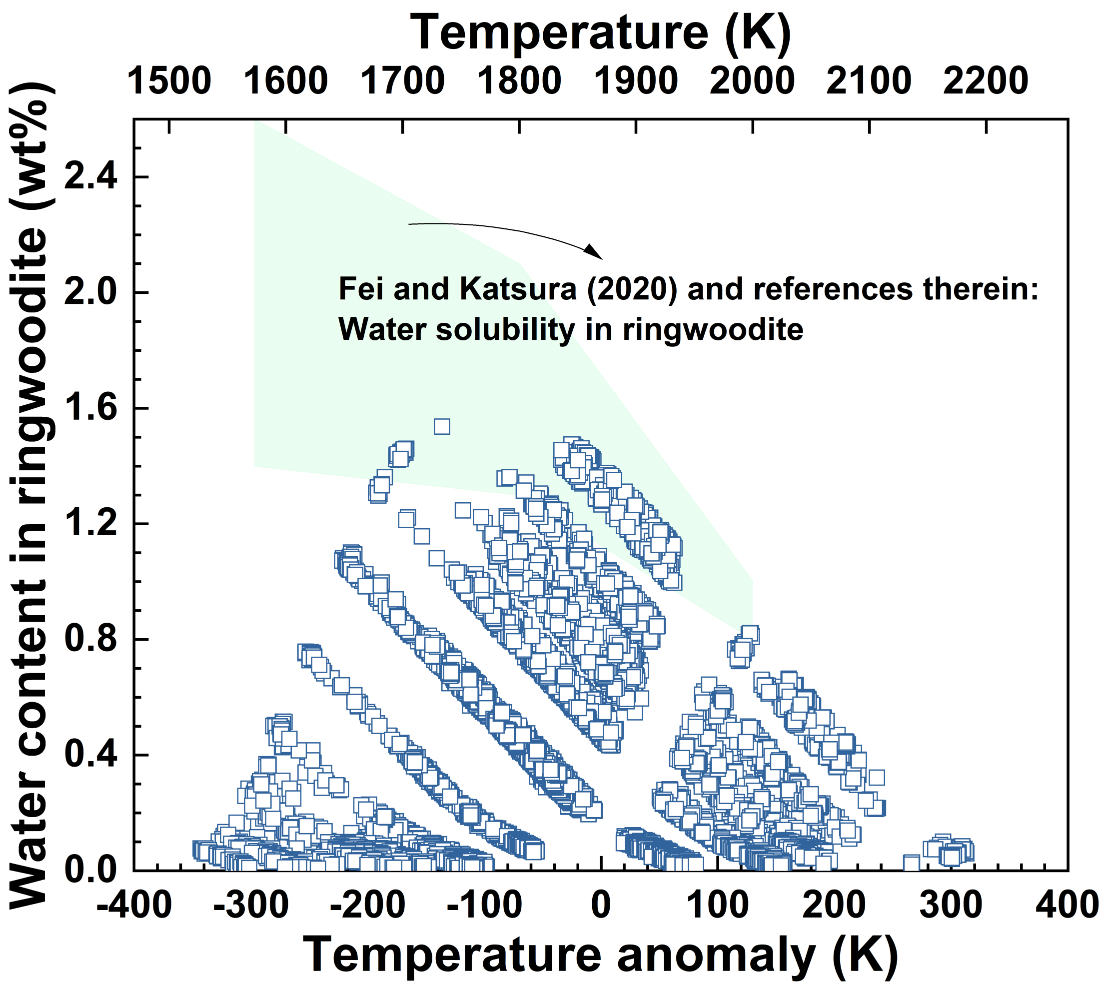

Figure S7. The water content in ringwoodite and temperature anomaly inferred from the depth variation of 660-km discontinuity and the shear velocity anomaly compared with the water solubility in ringwoodite (blue areas) from experimental measurements Fei and Katsura (2020).

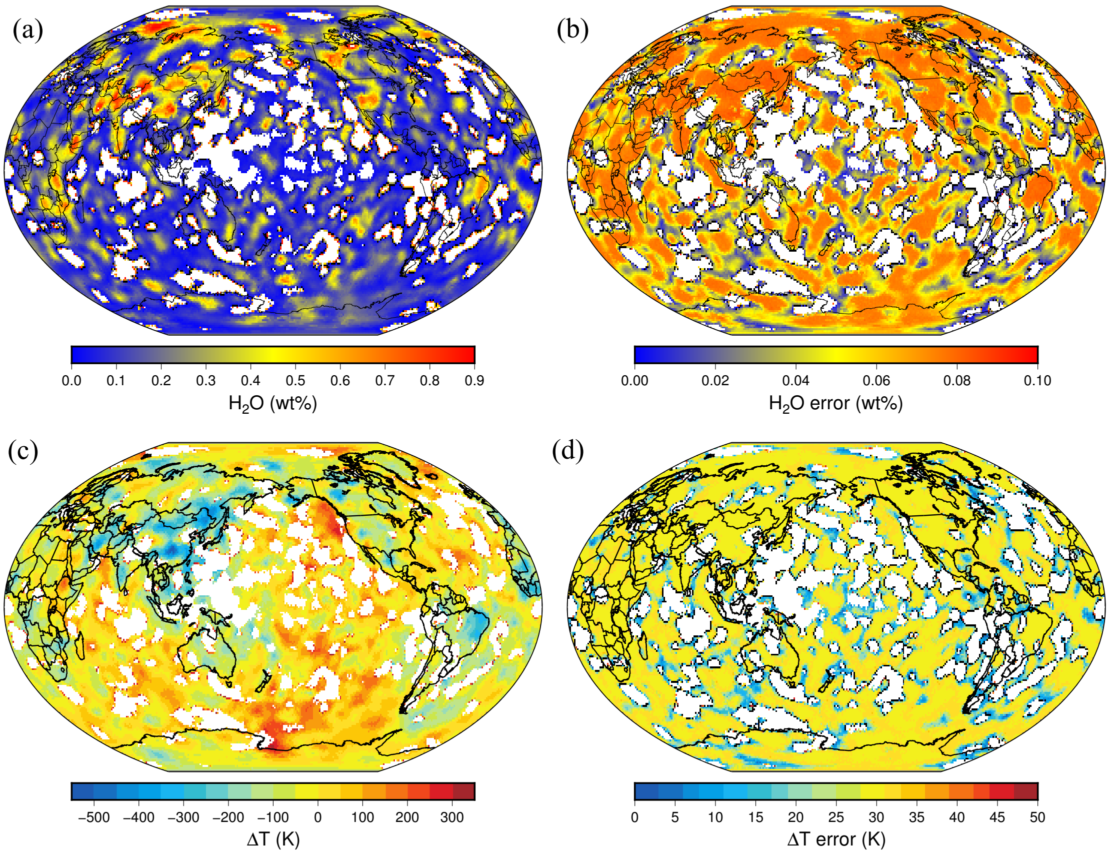

Figure S8. Water concentration (H_2O wt%) and temperature anomaly (ΔT (K)) in the lower MTZ inferred from the topography of 660-km discontinuity in Guo and Zhou (2020) and the shear velocity anomaly from the S40RTS model (Ritsema et al., 2011). (a) the map of water concentration and (b) the standard error of H_2O amount; (c) the map of temperature anomaly and (d) the standard error of ΔT.About 84% of the bins with ΔV_S and Δd can be explained by our models. The white areas are the remaining bins that are not consistent with the current mineral models. The average water concentration is 0.18±0.05 wt% and the average temperature anomaly is -23±26 K.